STATE OF THE CLIMATE IN 2011

Special Supplement to the
Bulletin of the American Meteorological Society
Vol. 93, No. 7, July 2012

STATE OF THE CLIMATE IN 2011

Editors

Jessica Blunden

Derek S. Arndt

Associate Editors

Howard J. Diamond

A. Johannes Dolman

Ryan L. Fogt

Margarita C. Gregg

Bradley D. Hall

Martin O. Jeffries

Michele L. Newlin

James A. Renwick

Jacqueline A. Richter-Menge

Ahira Sánchez-Lugo

Ted A. Scambos

Wassila M. Thiaw

Peter W. Thorne

Scott J. Weaver

Kate M. Willett

AMERICAN METEOROLOGICAL SOCIETY

4. THE TROPICS—H. J. Diamond, Ed.

a. *Overview*—H. J. Diamond

The year was characterized by two distinct La Niña episodes sandwiched around a period of ENSO-neutral conditions from April to August. The La Niña at the beginning of the year was of moderate strength with NOAA's Oceanic Niño Index (ONI) between -1.0°C and -1.4°C, while the La Niña the latter part of the year was weaker, with the ONI between -0.5°C and -0.9°C.

Overall, global tropical cyclone (TC) activity during 2011 was well-below normal, with a total of 74 storms the 1981–2010 global average is 89). This activity was only slightly higher than the record-low number of global TCs (since the start of the satellite era) set in 2010. Only the North Atlantic basin experienced above-normal activity in 2011. It was also the first year since the widespread introduction of the Dvorak intensity-estimation method in the 1980s when only three TCs globally briefly reached the Saffir-Simpson Category 5 intensity level, all in the Northwest Pacific basin.

This chapter consists of seven sections: (1) ENSO and the tropical Pacific; (2) Tropical intraseasonal activity; (3) seasonal TC activity in the seven TC basins: the North Atlantic, Eastern North Pacific, Western North Pacific, North Indian and South Indian Oceans, Southwest Pacific, and Australia; (4) TC heat potential, which aids in summarizing the section for TCs from an ocean heat perspective; (5) Intertropical convergence zone (ITCZ) behavior in the Pacific and Atlantic basins; and (6) the Indian Ocean dipole (IOD). A section detailing the Atlantic Multidecadal Oscillation (AMO) complements some of the other work related to Atlantic hurricane activity, ENSO, the IOD, and the Madden-Julian oscillation (MJO). In picking up on some information published in last year's report on the use of indigenous knowledge related to tropical activity in the South Pacific, a sidebar on the use of indigenous knowledge as an indicator for tropical cyclone activity in Polynesia is included in this year's chapter.

b. *ENSO and the tropical Pacific*—M. L'Heureux, M. Halpert, and G. D. Bell

1) Oceanic conditions

The El Niño-Southern Oscillation (ENSO) is a coupled ocean-atmosphere phenomenon over the tropical Pacific Ocean. Opposite warm and cool phases of ENSO, called El Niño and La Niña, respectively, are classified by NOAA's Climate Prediction Center (CPC) using the Niño-3.4 index, which is based on the area-averaged sea surface temperature (SST) anomalies in the east-central equatorial Pacific (5°N–5°S, 170°W–120°W). The Oceanic Niño Index (ONI) is a three-month running average of the Niño-3.4 index and is used by NOAA to classify ENSO events historically[1].

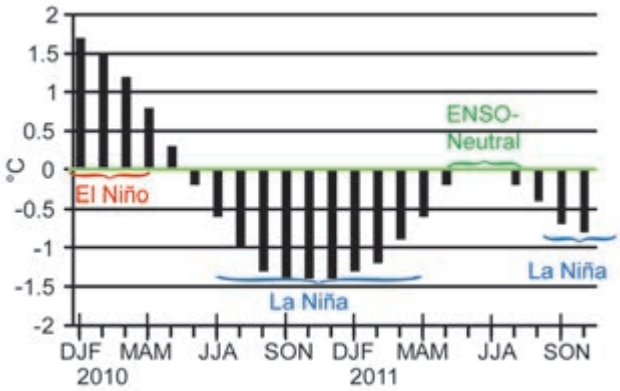

Fig. 4.1. Time series of the Oceanic Niño Index (ONI, °C) during DJF 2010/11 through OND 2011. The data are derived from the ERSST-v3b dataset (Smith et al. 2008).

A time series of the ONI shows two distinct La Niña episodes during 2011 (Fig. 4.1). The first lasted from June–August (JJA) 2010 through March–May (MAM) 2011, reaching moderate strength (ONI between -1.0°C and -1.4°C) between July–September (JAS) 2010 and January–March (JFM) 2011. ENSO-neutral conditions then prevailed from April–June (AMJ) to August–October (ASO) 2011, followed by a return to weak La Niña conditions through the end of the year (ONI between -0.5°C and -0.9°C).

The spatial structure and evolution of the tropical Pacific SSTs and anomalies during 2011 are shown in Fig. 4.2. During December 2010–February 2011 (DJF), La Niña conditions were associated with an enhanced equatorial cold tongue that extended from the west coast of South America to the International Date line (hereafter date line)[2], and with a westward retraction in the area of warmest SSTs (> 30°C) to the area north of New Guinea (Fig. 4.2a). Negative SST anomalies cooler than -1.0°C extended across the cen-

[1] For historical purposes, the CPC classifies an El Niño (La Niña) episode when the ONI is greater (less) than or equal to +0.5°C (-0.5°C) for five consecutive overlapping seasons (as measured by the ERSST-v3b dataset using 1971–2000 monthly mean normals, Smith et al. 2008).

[2] The date line has no physical significance as it merely traverses around the Antimeridian at 180° longitude, but is still a useful and popularly used reference point for describing activity in the tropics.

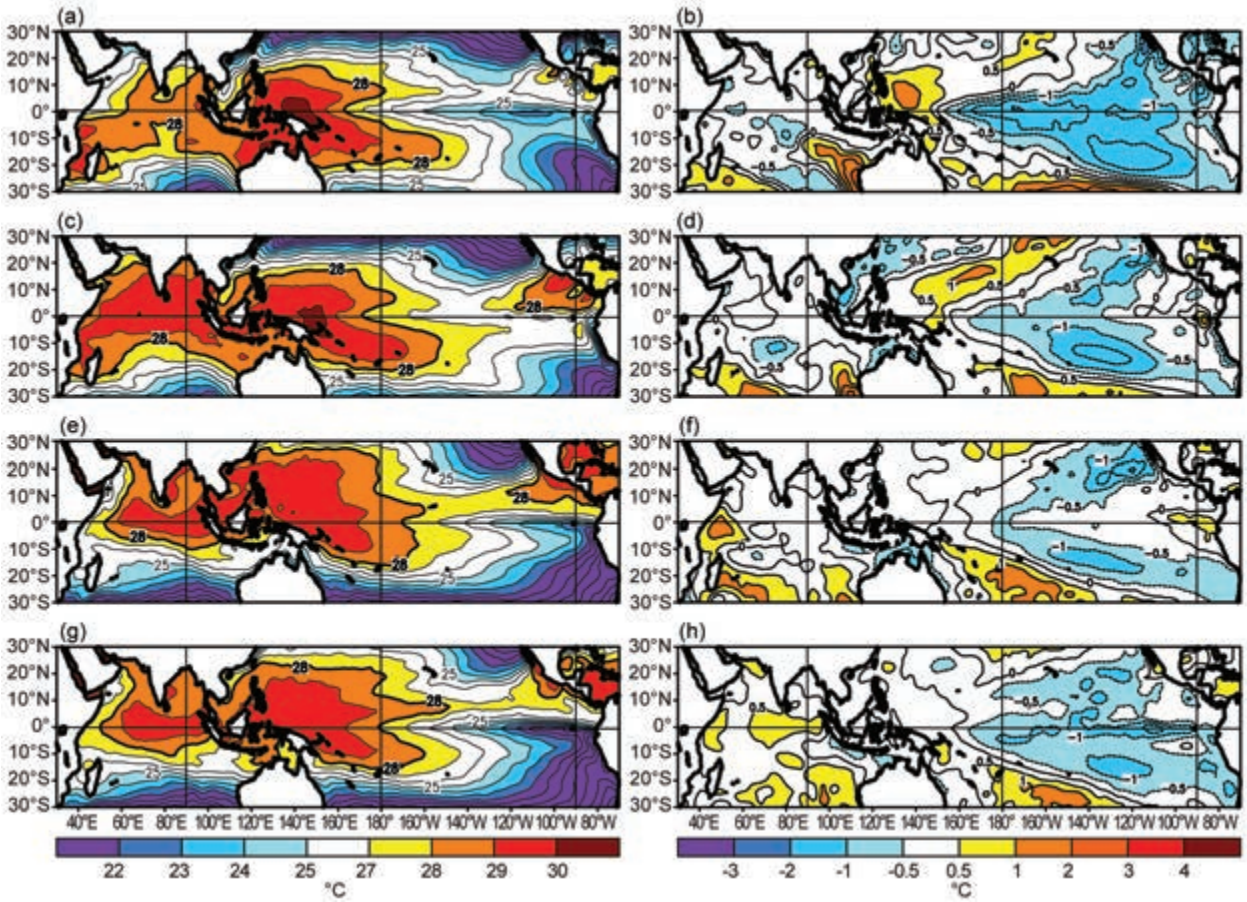

Fig. 4.2. Seasonal SSTs (left) and anomalies (right) for (a) and (b) DJF 2010/11, (c) and (d) MAM 2011, (e) and (f) JJA 2011 and (g) and (h) SON 2011. Contour interval for total (anomalous) SST is 1°C (0.5°C). Anomalies are departures from the 1981–2010 seasonal-adjusted Optimum Interpolation (OI) SST climatology (Smith and Reynolds 1998).

tral and eastern equatorial Pacific, and throughout the subtropical eastern Pacific in both hemispheres (Fig. 4.2b). Conversely, SSTs were above average in the western equatorial Pacific and portions of the western subtropical Pacific of both hemispheres. The resulting horseshoe-shaped anomaly pattern is typical of La Niña.

During MAM, La Niña became weak (ONI of -0.6°C) as SST anomalies weakened throughout the tropical Pacific and conditions returned to near-average in the eastern Pacific (Figs. 4.2c,d). This evolution is consistent with the 1950–2010 trend during boreal springtime La Niña events, which favors relatively warmer conditions in the eastern equatorial Pacific and relatively cooler conditions in the central Pacific (L'Heureux et al. 2012).

During JJA, ENSO-neutral conditions were present, with near-average SSTs observed across much of the central and east-central equatorial Pacific (Figs. 4.2e,f). However, large regions of below-average SSTs persisted in the off-equatorial central and eastern Pacific. By September–November (SON), a weak La Niña had returned (ONI of -0.7°C) as the equatorial cold tongue again became stronger than average (Fig. 4.2g) and SST anomalies colder than -1.0°C covered the eastern equatorial Pacific (Fig. 4.2h).

Consistent with the above evolution, the subsurface temperature structure varied considerably during the year (Fig. 4.3). In DJF, temperatures were below average from the surface to 150 m depth east of 160°W, and above average (anomalies exceeding +4°C) in the western Pacific between 100 m and 200 m depth (Fig. 4.3a). This overall anomaly pattern is typical of La Niña, and reflected a shallower- (deeper-) than-average thermocline in the eastern (western) Pacific.

During MAM, subsurface temperatures returned to near average across the eastern half of the equatorial Pacific and the area of above-average temperatures expanded eastward (Fig. 4.3b). This evolution reflected the transition to ENSO-neutral conditions that began in AMJ, partly in association with the

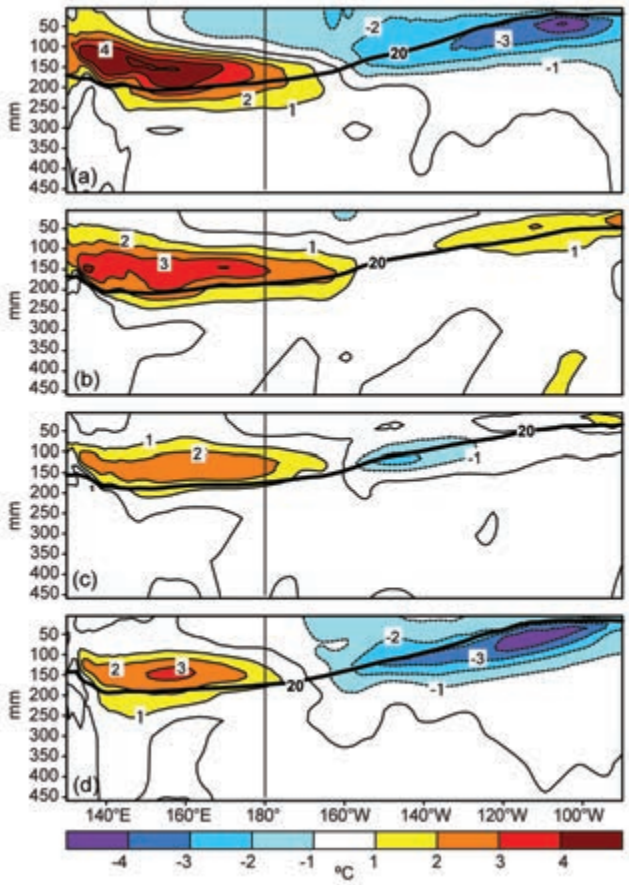

Fig. 4.3. Equatorial depth–longitude section of ocean temperature anomalies (°C) averaged between 5°N and 5°S during (a) DJF 2010/11, (b) MAM 2011, (c) JJA 2011, and (d) SON 2011. The 20°C isotherm (thick solid line) approximates the center of the oceanic thermocline. The data are derived from an analysis system that assimilates oceanic observations into an oceanic global circulation model (Smith et al. 2008). Anomalies are departures from the 1981–2010 period monthly means.

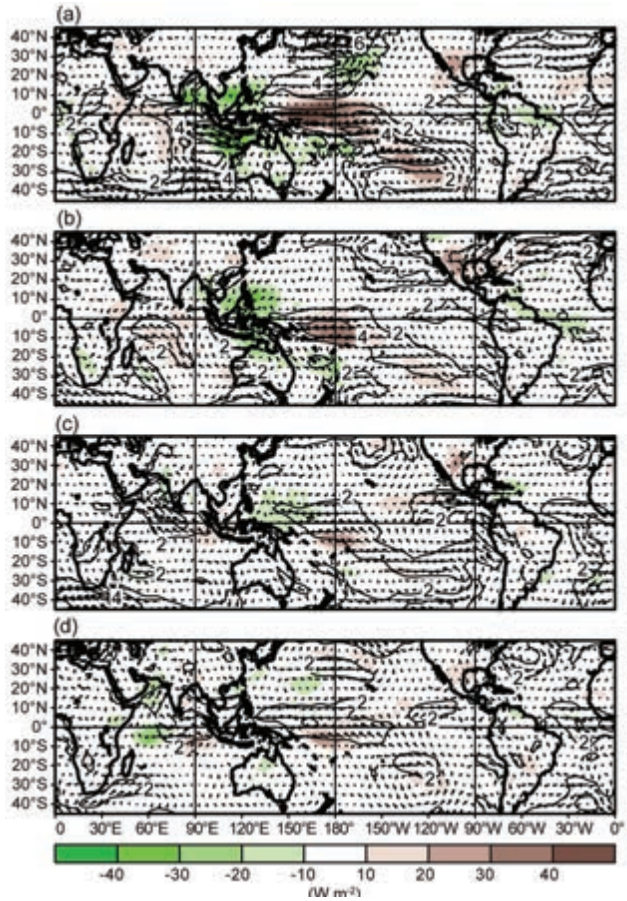

Fig. 4.4. Anomalous 850-hPa wind vector and speed (contours, m s^{-1}) and anomalous OLR (shaded, W m^{-2}) during (a) DJF 2010/11, (b) MAM 2011, (c) JJA 2011, and (d) SON 2011. Anomalies are departures from the 1981–2010 period monthly means.

downwelling phase of a strong equatorial oceanic Kelvin wave (see section 4c). By SON, the subsurface temperature pattern again reflected an increased east-west thermocline gradient more reminiscent of conditions during DJF, heralding the return of La Niña (Fig. 4.3d).

2) Atmospheric circulation: Tropics

Although SSTs and subsurface temperatures in the equatorial Pacific were near average during the boreal summer, many aspects of the tropical atmospheric circulation retained their La Niña characteristics. As a result, the low-level 850-hPa trade winds in the western and central equatorial Pacific (west of 150°W) were enhanced throughout the year, as was the cross-equatorial flow over the eastern Pacific (Fig. 4.4).

Additionally, westerly wind anomalies prevailed at 200 hPa throughout the year across the central equatorial Pacific, as did a cyclonic circulation couplet straddling the equator (near 150°W) in the subtropics of both hemispheres (Fig. 4.5). These conditions were associated with below-average precipitation near the date line in all seasons (brown shading in Figs. 4.4, 4.5). Collectively, they reflected well-known La Niña-related features such as an enhanced equatorial Walker circulation and a suppressed Hadley circulation over the central Pacific.

While the large-scale tropical atmospheric circulation retained general La Niña characteristics throughout the year, there were some notable circulation differences among the seasons. The pattern of enhanced convection over Indonesia (green shading) and suppressed convection over the west-central equatorial Pacific was strongest during DJF as mature La Niña conditions developed (shading in Figs. 4.4a, 4.5a). The region of suppressed convection near the

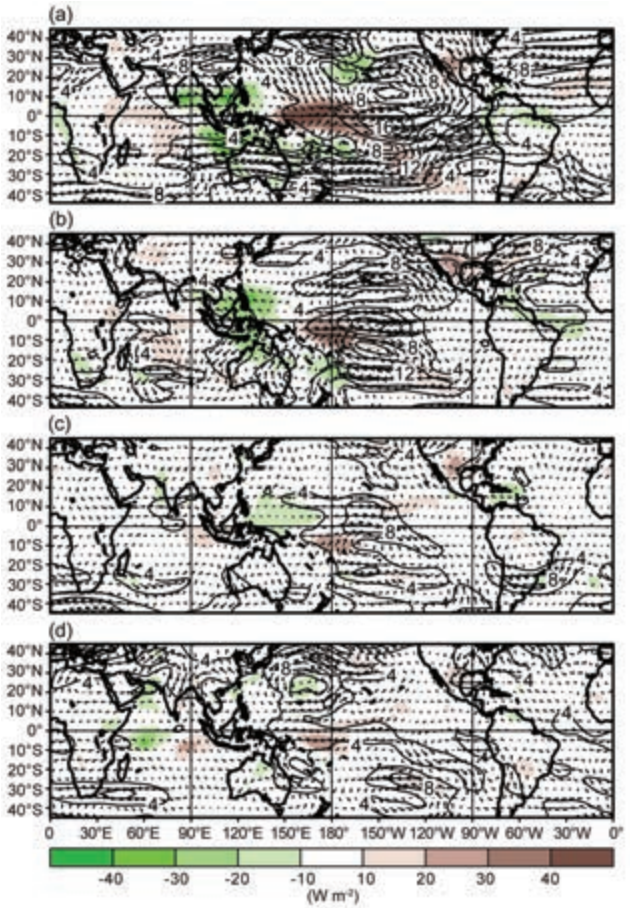

Fig. 4.5. Anomalous 200-hPa wind vector and speed (contours, m s^{-1}) and anomalous OLR (shaded, W m^{-2}) during (a) DJF 2010/11, (b) MAM 2011, (c) JJA 2011, and (d) SON 2011. Anomalies are departures from the 1981–2010 period monthly means.

date line was weakest during the second half of the year, even as La Niña reemerged (Figs. 4.4c,d; 4.5c,d). The enhanced convection near Indonesia gradually weakened into JJA (Figs. 4.4c, 4.5c), and by SON had become near to below average across the region (Figs. 4.4d, 4.5d).

Consistent with the declining strength of the convective anomalies through the year, the anomalous 200-hPa equatorial westerlies over the tropical Pacific were also strongest during DJF (Fig. 4.5a) and weakest during SON (Fig. 4.5b). The anomalous cyclonic circulation anomalies in the subtropics of both hemispheres, located just to the east of suppressed convection, also weakened as the year progressed.

At 850 hPa, the anomalous low-level easterlies were strongest during MAM (Fig. 4.4b) and remained close to their peak intensity though the rest of the year, although the core of the largest anomalies shifted into the western equatorial Pacific during JJA and SON (Figs. 4.4c,d).

3) Atmospheric circulation: Extratropics

While the strongest extratropical anomalies associated with La Niña occurred during DJF and MAM, an anomalous anticyclone was evident over the extratropical central-to-eastern North Pacific Ocean throughout the year (see Figs. A1.2–A1.5). This feature likely reflected the persistence of below-average convection over the central equatorial Pacific.

The position of the East Asian jet stream (located 30°N–40°N) is sensitive to the location of anomalous convective heating during ENSO and to the associated subtropical circulation anomalies. During La Niña, the lack of convection over the central equatorial Pacific and increased convection over Indonesia causes a westward retraction of the East Asian jet stream to west of the date line, along with a westward shift and amplification of the jet exit region.

This jet structure favors an anomalous westward shift in the downstream ridge axis normally located over western North America. Such a shift during 2011 was indicated by the lack of a mean ridge over western North America throughout the year, along with the anomalous anticyclone over the central and eastern North Pacific.

Another indication of this westward shift during DJF (see Fig. A1.2) was the presence of a mean upper-level ridge in the vicinity of the climatological mean Aleutian Low. Over the United States, this anomalous circulation translated into a storm track that was shifted north of normal, and contributed to above-average precipitation across the northern US and below-average precipitation across the southern US.

ENSO often occurs in combination with other climate factors or teleconnection patterns, such as the Arctic Oscillation (AO) or North Atlantic Oscillation (NAO), and the tropical multidecadal signal or AMO (see section 4d2). For example, while the 500-hPa circulation over the North Pacific during DJF reflected characteristics of La Niña, the larger-scale hemispheric circulation showed strong links to the negative phase of the AO/NAO.

As this AO pattern dissipated, the 500-hPa heights near Hudson Bay flipped from above average during DJF to below average during MAM (Fig. A1.3). Also during this period, the axis of the anomalous North Pacific ridge shifted eastward from the Aleutian Islands, near the date line, to 150°W. Downstream, the anomalous trough over the northwestern US and western Canada strengthened considerably during MAM. Over North America, this evolution contributed to temperature and precipitation patterns dur-

ing MAM that more closely resembled the canonical wintertime La Niña signal.

La Niña also affected the circulation over the South Pacific Ocean. For example, the anticyclonic anomalies over the central subtropical South Pacific reflected a strengthening of the normal mid-Pacific trough and a westward retraction of the ridge axis to the extreme western Pacific. These conditions were associated with easterly 200-hPa wind anomalies across the central Pacific near 30°S, which coincided with the exit region of the South Pacific jet core (Fig. 4.5) and therefore mirrored the weakening and westward retraction of the East Asian jet to west of the dateline.

4) ENSO TEMPERATURE AND PRECIPITATION IMPACTS

During DJF and MAM, the precipitation patterns typically associated with La Niña (Ropelewski and Halpert 1989; see also http://www.cpc.ncep.noaa.gov/products/precip/CWlink/ENSO/regressions/) were observed over many parts of the world. These included below-average precipitation over the equatorial western and central Pacific Ocean, much of the southern tier of the contiguous United States, the Horn of Africa, and southeastern South America. Impacts also included above-average precipitation over northern Australia, Indonesia, the Philippines, Southeast Asia, and northeastern South America.

La Niña-related temperature impacts during DJF and MAM included cooler-than-average conditions over northern Australia, the west coast of South America, and the northwestern and north-central United States extending into Canada and Alaska. During DJF, cooler-than-average conditions across parts of the northern US were influenced by the negative phase of the AO/NAO.

c. *Tropical intraseasonal activity*—J. Gottschalck and G. D. Bell

The Madden-Julian oscillation (MJO; Madden and Julian 1971, 1972, 1994; Zhang 2005) is a leading climate mode of tropical convective variability that occurs on intraseasonal timescales. The convective anomalies associated with the MJO often have the same spatial scale as ENSO, but differ in that they exhibit a distinct eastward propagation and generally traverse the globe in 30–60 days. The MJO can strongly affect the tropical and extratropical atmospheric circulation patterns, and may produce ENSO-like anomalies (Mo and Kousky 1993; Kousky and Kayano 1994; Kayano and Kousky 1999). The MJO is often quite variable in a given year, with periods of moderate-to-strong activity sometimes followed by little or no activity. Overall, the MJO tends to be most active during neutral and weak ENSO periods, and is often absent during strong El Niño events (Hendon et al. 1999; Zhang and Gottschalck 2002; Zhang 2005).

The MJO is seen by continuous eastward propagation of 200-hPa velocity potential anomalies around the globe. A time-longitude section of this parameter shows three periods during 2011 with MJO activity (Fig. 4.6). These include: (1) a short-lived episode during January (MJO #1); (2) moderate-strength activity during March to mid-May (MJO #2); and (3) strong activity from late September to early December (MJO #3). There was little MJO activity during the summer, when the intraseasonal variability was often dominated by higher frequency and faster propagating

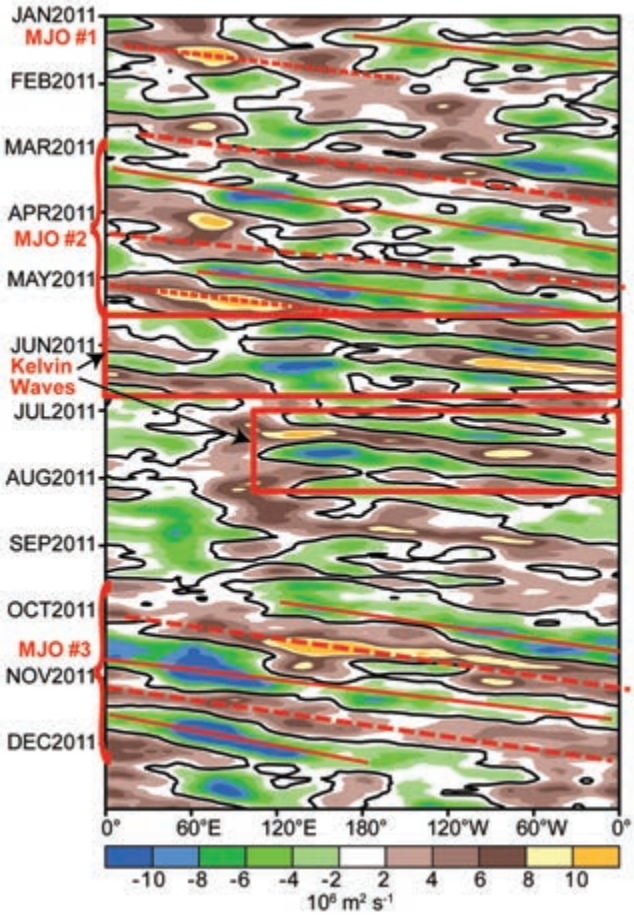

Fig. 4.6. Time–longitude section for 2011 of anomalous 200-hPa velocity potential ($\times 10^6$ m^2 s^{-1}) averaged between 5°N and 5°S. For each day, the period mean is removed prior to plotting. Green (brown) shading highlights likely areas of anomalous divergence and rising motion (convergence and sinking motion). Red lines and labels highlight the main MJO episodes. The June–August atmospheric Kelvin wave activity is also indicated. Anomalies are departures from the 1981–2010 base period daily means.

atmospheric Kelvin waves (Wheeler and Kiladis 1999; Wheeler and Weickmann 2001).

The first period of MJO activity (MJO #1) featured the eastward propagation of enhanced equatorial convection (green shading) across the Western Hemisphere and suppressed convection (brown shading) across the Eastern Hemisphere. Although this activity was generally short-lived, it caused a significant weakening of the low-level trade winds across the western Pacific, which helped to trigger a downwelling oceanic Kelvin wave (Roundy and Kiladis 2006) in late January (Fig. 4.7, dashed line). This oceanic Kelvin wave acted to increase the subsurface temperatures in the central and eastern Pacific during March and April as it approached the South American coast, thereby contributing to the weakening of the 2010/11 La Niña episode. This was the only appreciable downwelling oceanic Kelvin wave of the year.

A longer period of MJO activity began in early March and lasted well into May (MJO #2), with the most robust convective signatures seen during March and early May. Two complete cycles were evident during this three-month period, as seen by multiple traverses around the globe of the areas of enhanced and suppressed convection. Although these propagating anomaly patterns continued into June, their forward speed and spatial scale at that time became more characteristic of higher-frequency atmospheric Kelvin wave activity.

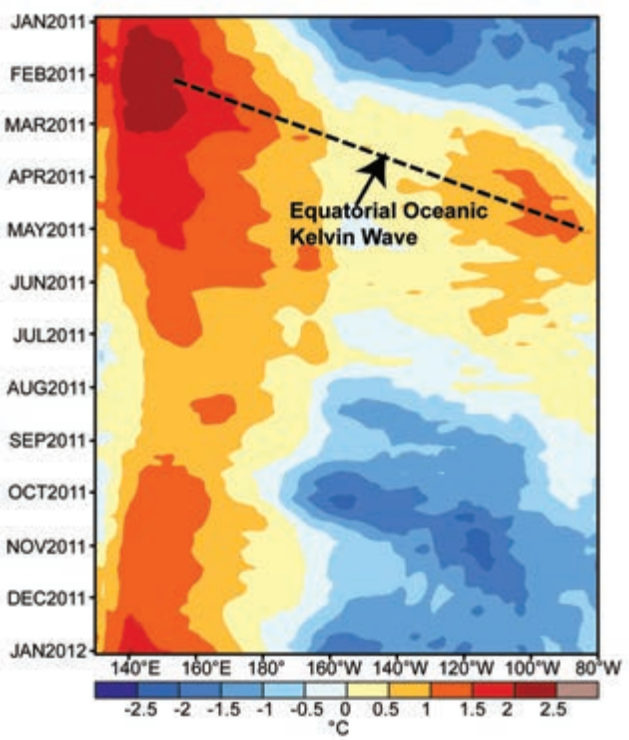

Fig. 4.7. Time–longitude section for 2011 of the anomalous upper ocean (0 m – 300 m) heat content (°C) averaged between 5°N and 5°S. Blue (yellow/red) shading indicates below- (above-) average heat content. The downwelling phases (dashed lines) of equatorial oceanic Kelvin waves are indicated. Anomalies are departures from the 1981–2010 base period means.

The third period of MJO activity occurred from late September to early December (MJO #3), and reflected the strongest and longest MJO episode since October 2007–February 2008 (Gottschalck and Bell 2009). The MJO again displayed two successive complete cycles, with the enhanced convective phase over the Maritime Continent in late September shifting eastward and returning to this region in early November and again in early December. The periods of the two cycles to traverse the global tropics were approximately 45 and 30 days, respectively. The enhanced convective phase of the first cycle, during its time in the Western Hemisphere, contributed to the development of favorable conditions over the Atlantic basin for the formation of Major Hurricane Rina in mid-October.

Convection was particularly intense over the Indian Ocean during late October/early November and again in late November/early December. The initiation and continuation of this strong MJO activity coincided with the Intensive Observing Period (IOP) of the Dynamics of the MJO (DYNAMO) field campaign, whose objective was to better understand the mechanisms of MJO onset and maintenance. Consequently, this MJO activity was well sampled by various in situ measurements, the NOAA P3 aircraft, and two ship research vessels.

d. Tropical cyclones

1) Overview—H. J. Diamond and B. C. Trewin

The International Best Track Archive for Climate Stewardship (IBTrACS) comprises historical tropical cyclone best-track data from numerous sources around the globe, including all of the Regional Specialized Meteorological Centers (RSMC; Knapp et al. 2010). To date, IBTrACS represents the most complete compilation of tropical cyclone data and offers a unique opportunity to revisit the global climatology of tropical cyclones. Using IBTrACS data (Schreck et al. 2012), a 30-year average value for storms (based upon WMO-based RSMC numbers) will be noted for each basin.

The global tallying of total tropical cyclone (TC) numbers is challenging and involves more than simply adding up basin totals because some storms cross

basin boundaries, some basins overlap, and multiple agencies are involved in tracking and forecasting TCs. Compiling the activity over all seven TC basins, the 2011 season (2010/11 in the Southern Hemisphere) saw a well-below-average (1981–2010 base period) number of named storms (NS; wind speeds ≥ 34 kts or 17.5 m s^{-1}) and hurricanes/typhoons/cyclones (HTC; wind speeds ≥ 64 kts or 32.9 m s^{-1}) and an above-average number of major HTCs (wind speeds ≥ 96 kts or 49.4 m s^{-1}). Globally, 74 named storms[3] developed during the 2011 season (global average is 89), with 38 becoming HTCs (global average is 44). Of these, 22 (compared to 26 in 2006, 18 in 2007, 20 in 2008, 16 in 2009, and 22 in 2010) attained major/intense status (global average is 19). Therefore, while the overall NS count was well-below average, the number of major/intense storms was above the IBTrACS global average.

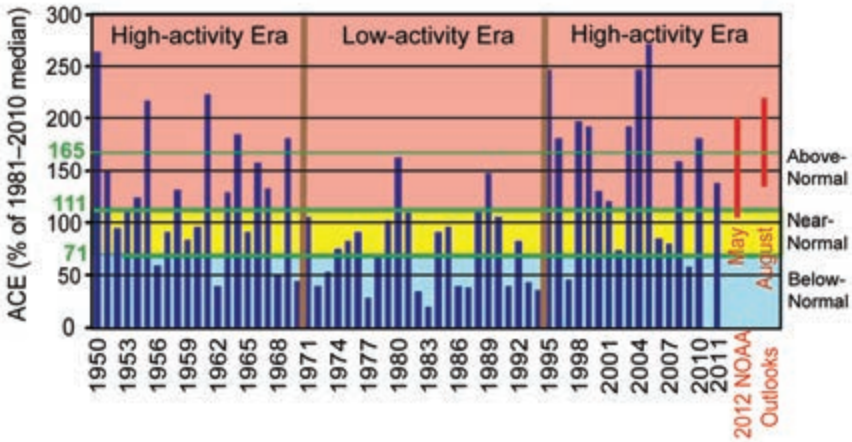

Fig. 4.8. NOAA's ACE index expressed as percent of the 1981–2010 median value. ACE is calculated by summing the squares of the six-hourly maximum sustained wind speed (knots) for all periods while the storm has at least tropical storm strength. Red bars show NOAA's predicted ACE ranges in their May and August seasonal hurricane outlooks. Pink, yellow, and blue shadings correspond to NOAA's classifications for above-, near-, and below-normal seasons, respectively. The 165% threshold for a hyperactive season is indicated. Vertical brown lines separate high- and low-activity eras.

On the whole, while global tropical cyclone activity was again below normal in 2011, it was higher than in 2010, which set the record for the lowest number of global TCs since the start of the satellite era. There were no clear-cut Category 5 systems during the year, an unusual occurrence, with the year's most intense systems: (1) Adrian, Dora, Eugene, Hilary, and Kenneth in the Northeast Pacific; (2) Ophelia in the North Atlantic; (3) Nanmadol, Songda, and Muifa in the Northwest Pacific; and (4) Yasi in the Australian region, all peaking at Category 4[4].

The only basin which had substantially above-normal activity in 2011 was the North Atlantic, where elevated TC activity is a typical response to La Niña has been seen in 12 of the last 17 seasons since 1995. Conversely, the South Indian, North Indian, and Northeast Pacific basins experienced well-below-normal TC numbers (although the Northeast Pacific had an above-normal average number of hurricanes and major hurricanes). Part of the explanation for the low global number of tropical cyclones was that the characteristic La Niña boost to numbers in the Australian region, which would normally offset La Niña-induced deficits in many other hurricane regions, was absent in 2011, with both the Australian region and the Southwest Pacific basins experiencing near-normal activity.

2) Atlantic basin—G. D. Bell, E. S. Blake, C. W. Landsea, T. B. Kimberlain, S. B. Goldenberg, J. Schemm, and R. J. Pasch

(i) 2011 Seasonal activity

The 2011 Atlantic hurricane season produced 19 tropical storms (TS), of which 7 became hurricanes and 4 became major hurricanes. The 30-year IBTrACS seasonal averages are 11.9 named storms, 6.4 hurricanes, and 2.7 major hurricanes (MH). The August–October (ASO) period is typically the peak of the season, and all but five named storms during 2011 formed in ASO.

The 2011 seasonal Accumulated Cyclone Energy (ACE) value (Bell et al. 2000) was 126.3×10^4 kt^2, which corresponds to 137% of the 1981–2010 median (Fig. 4.8). NOAA classifies the 2011 season as above normal (http://www.cpc.ncep.noaa.gov/products/outlooks/background_information.shtml). This is the 12th above-normal season since the current high activity era for Atlantic hurricanes began in 1995

[3] It should be noted that in the Western North Pacific there were an additional seven unnamed tropical depressions recorded by the Japan Meteorological Agency (JMA) that were not included in this total.

[4] Typhoons Songda and Muifa were classified as Category 5 operationally by the Joint Typhoon Warning Center but Category 4 in the best-track dataset produced by Japan Meteorological Agency, the responsible World Meteorological Organization center for the Northwest Pacific.

(Goldenberg et al. 2001), and the 14th busiest season since 1966. NOAA's seasonal hurricane outlooks, issued in late May and early August (http://www.cpc.ncep.noaa.gov/products/outlooks/hurricane-archive.shtml) by the CPC, indicated a high likelihood of an above-normal 2011 season (red bars).

Four global climate factors influenced the 2011 Atlantic hurricane season. Three of these contributed to more conducive conditions within the Main Development Region (MDR), including the active-Atlantic phase of the tropical multidecadal signal (sections 4d2*vi* and 4g of this report, and Bell and Chelliah 2006); La Niña (discussed in section 4b); and anomalously warm SSTs in the MDR (section 4d2*iv*). A fourth climate factor, the Indian Ocean dipole, may have acted to limit the overall activity for the 2011 season and is discussed in sections 4d2*viii* and 4h of this report.

(ii) Storm tracks

The Atlantic storm tracks during 2011 (Fig. 4.9, brown lines) were generally divided into three clusters. One cluster comprised six storms that formed over the central and eastern tropical Atlantic, which is the eastern half of the MDR (Fig. 4.9, green boxed region encompassing the tropical Atlantic Ocean and Caribbean Sea between 9.5°N and 21.5°N; Goldenberg et al. 2001). Five of these storms eventually became hurricanes (three became major) and three made landfall. Maria and Ophelia made landfall in Newfoundland, Canada, with tropical storm strength, and Irene made landfall as a hurricane along the US Atlantic coast.

The second cluster consisted of six systems (four named storms and two hurricanes, with one becoming Major Hurricane Rina) that formed over the western Caribbean Sea and Bay of Campeche, regions that often see increased activity during La Niña (e.g., 1989, 1996, and 2010). Five of these six systems made landfall as tropical storms, with only Don weakening to a tropical depression before moving over southeastern Texas. Arlene and Nate struck Mexico; Harvey made landfall in Belize and Mexico; Lee came ashore in south-central Louisiana, and Rina struck the Yucatan Peninsula.

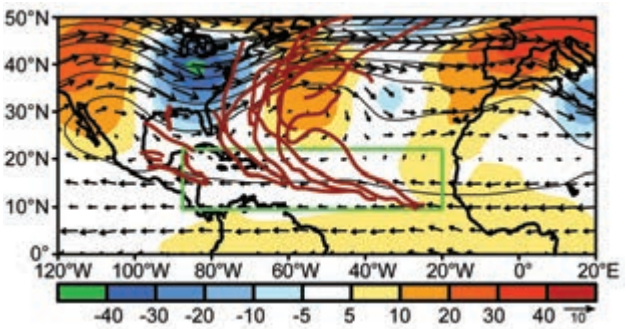

Fig. 4.9. ASO 2011: 500-hPa heights (contours, m), anomalies (shading), and layer mean wind vectors (m s^{-1}) between 600 hPa and 300 hPa. Atlantic named storm tracks are shown in brown. Green box denotes the MDR. Vector scale is below right of color bar. Anomalies are with respect to the 1981–2010 period monthly means.

The third cluster of tracks consisted of seven tropical storms that formed north of the MDR over the subtropical North Atlantic, and remained at sea throughout their life cycle (though Jose and Sean did pass close to Bermuda). This is one of the largest number of baroclinically-initiated (i.e., not from tropical waves) tropical storms since the satellite era began. On average, three to four named storms form over the subtropical North Atlantic per season and roughly two become hurricanes (McTaggart-Cowan et al. 2008; Kossin et al. 2010).

(iii) Hurricane landfalls

Irene was the first US hurricane landfall since 2008. This storm initially made US landfall in North Carolina (after making landfall in the Bahamas as a major hurricane), and then made another landfall as a tropical storm in New Jersey, subsequently causing major flooding in the Northeast. Irene was the most significant hurricane to strike the northeastern US since Hurricane Bob in 1991.

An analysis of the low US hurricane landfall frequency during 2009–11 (e.g., only one landfall in three seasons) was performed. The lack of landfalls during the below-normal 2009 season (Bell et al. 2010), and the occurrence of one landfall during the above-normal 2011 season, are consistent with past seasons of similar strength, although at the lower end of the distribution (Blake et al. 2011). However, the lack of hurricane landfalls during the hyperactive 2010 season (ACE > 165% of the median) is quite anomalous (Bell et al. 2011), as all previous hyperactive seasons had featured at least one US landfall, 92% had at least two landfalls, and 67% had at least three landfalls.

Two main atmospheric factors known to limit US hurricane landfalls were present during both 2010 and 2011: (1) a persistent mid-level trough and strong southwesterly flow over the western North Atlantic (Fig. 4.9) which steered all but one approaching hurricane (Irene) away from the US Atlantic coast; and (2) the absence of hurricanes either forming or

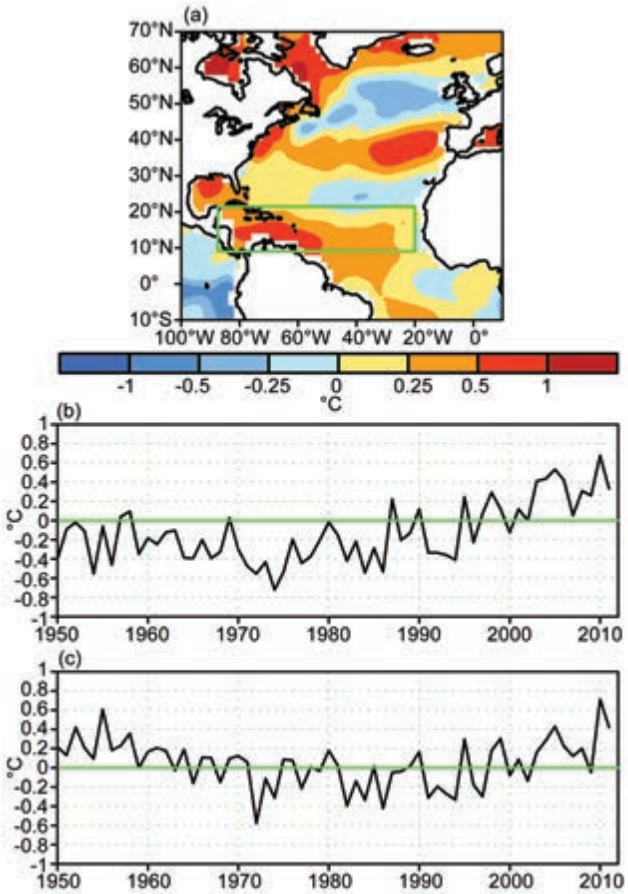

Fig. 4.10. (a) ASO 2011 SST anomalies (°C). (b) Time series of consecutive ASO area-averaged SST anomalies in the MDR [green box in (a)]. (c) Time series showing the difference between ASO area-averaged SST anomalies in the MDR and those for the entire global tropics (30°N–30°S). Anomalies are departures from the ERSST-v3b (Smith et al. 2008) 1981–2010 period monthly means.

propagating over the central and northern Gulf of Mexico. Historically, 50% of above-normal seasons have previously featured at least one hurricane formation in these regions. Also, such seasons often feature hurricanes that move into the central Gulf from the Caribbean Sea, yet none took such a track during either 2010 or 2011.

(iv) Atlantic sea surface temperatures

Sea surface temperatures (SST) in the MDR were above average during August–October 2011, with the largest departures (between +0.5°C and +1.0°C) observed in the Caribbean Sea and western tropical North Atlantic (Fig 4.10a). The mean SST departure within the MDR was +0.33°C (Fig 4.10b), which is +0.44°C warmer than the average departure for the entire global tropics (Fig 4.10c). These conditions were partly responsible for the above-normal Atlantic hurricane season.

This anomalous warmth is related to weaker-than-average easterly trade winds (e.g., westerly anomalies) across the tropical Atlantic (Fig 4.11a). This combination of weaker trade winds and anomalously warm SSTs in the MDR (both of which typically become established prior to the start of the season) has generally prevailed since 1995 (Fig 4.11b) in association with the warm phase of the Atlantic Multidecadal Oscillation (AMO; Enfield and Mestas-Nuñez 1999) and the active Atlantic phase of the tropical multidecadal signal.

(v) Atmospheric circulation

The atmospheric circulation during ASO 2011 featured an interrelated set of conditions known to be exceptionally conducive for TC formation and inten-

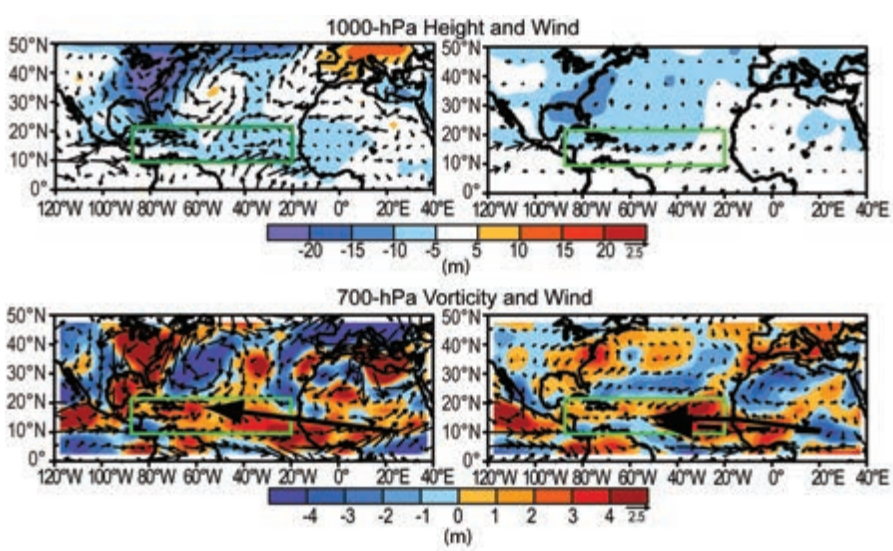

Fig. 4.11. (a) and (c) ASO 2011 anomalies and (b) and (d) difference between the 1995–2010 and 1971–1994 ASO means. Panels (a) and (b) show 1000-hPa heights (shading, m) and wind vectors (m s^{-1}). Panels (c) and (d) show 700-hPa relative vorticity (shading, $\times 10^{-6}$ s^{-1}) and wind vectors. In (c) thick arrow shows the axis of the African easterly jet (AEJ). In (d) thick solid (dashed) arrow indicates the mean position of the AEJ during 1995–2010 (1971–1994). Vector scales are below right of color bars. Green boxes denote the MDR. Anomalies are with respect to the 1981–2010 period monthly means.

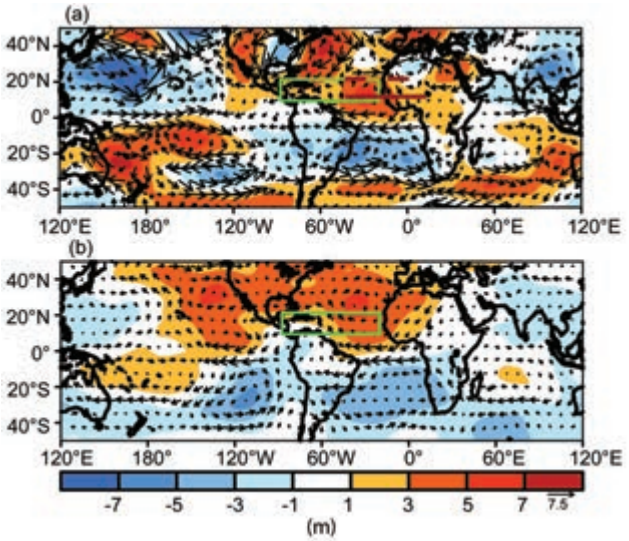

Fig. 4.12. 200-hPa streamfunction (shading, × 10^6 m^2 s^{-1}) and wind vectors (m s^{-1}). (a) Anomalies during ASO 2011 and (b) difference between 1995–2010 and 1971–1994 ASO means. In (a) brown solid (dashed) line over the eastern MDR shows location of mean ridge axis during ASO 2011 (ASO 1995–2010). Anomalous ridges are indicated by positive values (red) in the NH and negative values (blue) in the SH. Anomalous troughs are indicated by negative values in the NH and positive values in the SH. Green boxes denote the MDR. Vector scale is below right of color bar. Anomalies are with respect to the 1981–2010 base period monthly means.

sification within the MDR (Landsea et al. 1998; Bell et al. 2011; Goldenberg et al. 2001; Bell and Chelliah 2006; Kossin and Vimont 2007). Ten tropical storms formed in the MDR this year, eventually producing six of the seven total hurricanes, all major hurricanes, and 88% of the seasonal ACE value.

In the lower atmosphere, ASO conditions within the MDR included weaker trade winds, a deep layer of anomalous cross-equatorial flow, and below-average 1000-hPa heights (Fig. 4.11a, blue shading). Across the Atlantic basin and sub-Saharan Africa, the low-level westerly anomalies extended above 700 hPa, the approximate level of the African Easterly jet (AEJ; Fig. 4.11c), and were associated with an anomalous 2.5°–5° latitude northward shift of the AEJ core (black arrow, Fig. 4.11c).

As a result, the bulk of the African easterly wave energy (Reed et al. 1977) was often centered well within the MDR. The AEJ also featured increased cyclonic shear along its equatorward flank (Fig. 4.11c, red shading), which dynamically favors stronger easterly waves. These conditions have generally prevailed since 1995, and are opposite to those seen during the low activity era of 1971–94 (Fig 4.11d).

Also during ASO 2011, anomalous easterly flow at 200 hPa extended from the Gulf of Guinea to the eastern North Pacific (Fig 4.12a), although this flow was less extensive than seen in 2010. This pattern reflected a stronger and more westward extension of the tropical easterly jet, and occurred in association with enhanced upper-level ridges that spanned the entire subtropical Atlantic in both hemispheres. This interhemispheric symmetry is another prominent feature of the current high activity era (Fig. 4.12b).

The above circulation anomalies resulted in weaker vertical wind shear (less than 8 m s^{-1}) across the southern and western MDR (Fig 4.13), with the most anomalously weak shear located over the central tropical Atlantic and Caribbean Sea (Fig 4.13b). However, the area of anomalously weak shear was far less extensive than in 2010.

These conditions were part of the larger-scale pattern that included increased shear over both the eastern equatorial Atlantic and the eastern tropical North Pacific (Fig. 4.13b, blue shading), and are typical of other above-normal seasons since 1995 (Bell and Chelliah 2006; Bell et al. 2011). There was also an area of weaker-than-average shear over the northwestern Atlantic near Bermuda during ASO 2011, which could have helped promote the high number of named storms that formed in the subtropics.

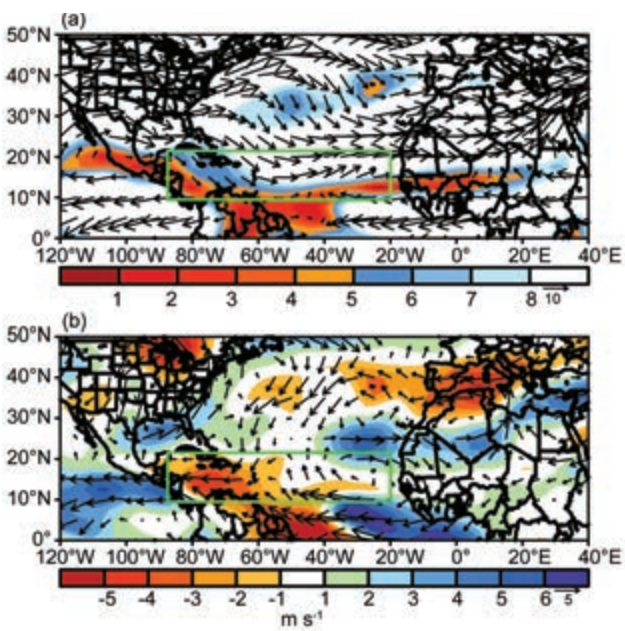

Fig. 4.13. ASO 2011 vertical wind shear magnitudes and vectors (m s^{-1}): (a) total and (b) anomalies. Green boxes denote the MDR. Vector scales are below right of color bars. Anomalies are with respect to the 1981–2010 period monthly means.

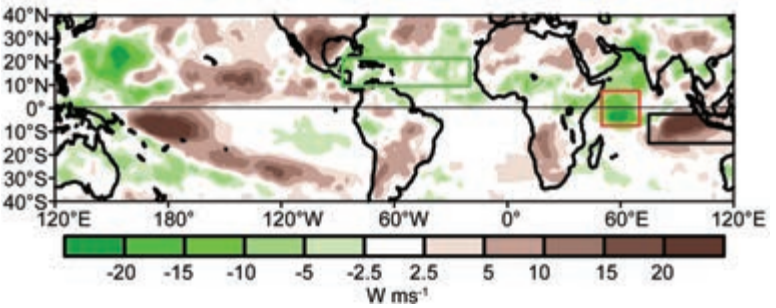

Fig. 4.14. ASO 2011 anomalous outgoing longwave radiation (OLR, W m^{-2}). Red (black) box denotes the western (eastern) portion of the Indian Ocean dipole (IOD). Green box denotes the MDR. Anomalies are with respect to the 1981–2010 period monthly means.

These circulation anomalies were accompanied by a stronger Atlantic ITCZ and enhanced convection across the MDR (Fig 4.14). They were also associated with an enhanced West African monsoon system, as indicated by enhanced convection across the African Sahel and Sudan regions and by a large area of negative velocity potential anomalies over northern Africa (Fig 4.15a). Similar anomaly patterns have been present throughout the current high activity era (Fig 4.15b).

For the Atlantic basin, the above conditions meant that many tropical storms formed within the MDR, primarily from easterly waves moving westward from Africa. These systems entered an extensive area of below-average pressure, deep tropical moisture, increased low-level convergence, and increased cyclonic shear south of the AEJ core-conditions known to be conducive for tropical cyclone formation. Many of these systems then generally strengthened while propagating westward within the extended region of weak vertical wind shear and anomalously warm SSTs.

(vi) The tropical multidecadal signal

Since 1995, more than 70% (12 of 17) of Atlantic hurricane seasons have been above normal, and only 2 have been below normal (Fig. 4.8). This elevated level of activity contrasts sharply with the 1971–94 low-activity era, when one-half of seasons were below normal and only three were above normal.

The sharp transition to the current high activity era reflected a phase change in the tropical multidecadal signal. This signal includes the leading modes of tropical convective rainfall variability and Atlantic SSTs occurring on multidecadal time scales (Bell and Chelliah 2006; Bell et al. 2007). It directly links atmospheric variability across the central and eastern MDR to multidecadal fluctuations in the strength of the West African monsoon system (Landsea and Gray 1992; Landsea et al. 1998; Bell et al. 2009; Goldenberg and Shapiro 1996; Goldenberg et al. 2001; Bell and Chelliah 2006; Kossin and Vimont 2007).

Between 1994 and 1995, the ocean-atmosphere system switched to the active Atlantic phase of the tropical multidecadal signal, which features an enhanced West African monsoon system (Fig. 4.15b) and above-average SSTs in the MDR (i.e., the warm phase of the AMO; Fig. 4.10). As a result, the atmospheric circulation within the MDR became much more conducive to Atlantic hurricane activity in 1995, as also indicated by the transition to weaker vertical wind shear (Fig. 4.16a), weaker 700-hPa zonal winds (Fig. 4.16b), and cyclonic (rather than anticyclonic) relative vorticity at 700 hPa across the southern MDR (Fig. 4.16c).

(vii) Indian Ocean dipole

The Indian Ocean dipole (IOD) reflects opposite patterns of anomalous tropical convection between the western and eastern Indian Ocean (Saji et al. 1999; Saji and Yamagata 2003a,b). A strong positive phase of the IOD was present during ASO 2011 (Fig. 4.17a), as indicated by enhanced convection over the western equatorial Indian Ocean and suppressed convection

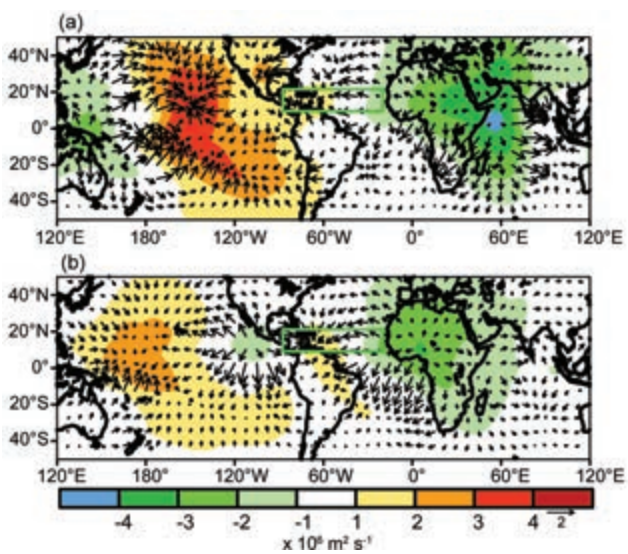

Fig. 4.15. 200-hPa velocity potential (shading, × 10^6 m^2 s^{-1}) and divergent wind vectors (m s^{-1}): (a) ASO 2011 anomalies and (b) difference between the 1995–2010 and 1971–94 ASO means. Green boxes denote the MDR. Vector scale is below right of color bar. Departures are with respect to the 1981–2010 period monthly means.

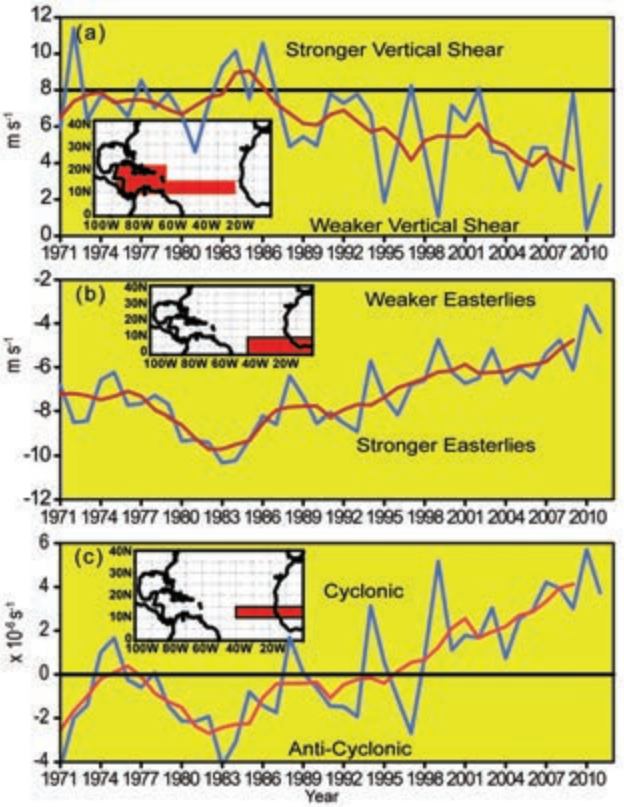

Fig. 4.16. Time series showing consecutive ASO values of area-averaged (a) 200-hPa–850-hPa vertical shear of the zonal wind (m s^{-1}), (b) 700-hPa zonal wind (m s^{-1}) and (c) 700-hPa relative vorticity ($\times$ 10^{-6} s^{-1}). Blue line shows unsmoothed values and red line shows a five-point running mean of the time series. Averaging regions are shown in the insets.

over the eastern tropical Indian Ocean (Fig. 4.14, red and black boxes, respectively).

There have been eight significant positive IOD events since reliable global outgoing longwave radiation (OLR) data became available in 1979. Figure 4.17b shows the Atlantic hurricane activity for these eight seasons. While these events have occurred during all phases of ENSO, they are typically associated with reduced Atlantic hurricane activity. The positive IOD event in 2011 may have been one reason why the overall Atlantic activity was lower (i.e., at the low end of the NOAA seasonal outlook issued in August, see Fig. 4.8) than what might have been expected given the combination of conducive climate factors present.

Specifically, the observations suggest that the IOD may have acted to limit the 2011 Atlantic hurricane activity by weakening both the West African monsoon circulation and the La Niña-related convection patterns. There are three indications of a weaker West African monsoon system compared to the 1995–2010 mean. First, the anomalous upper-level divergent circulation over northern Africa was weaker and less focused, and the anomalies were actually less than those over the western equatorial Indian Ocean (Fig. 4.15a). Second, the position of the 200-hPa subtropical ridge axis over the eastern MDR was located approximately 10° latitude farther south than the 1995–2010 mean (red lines, Fig. 4.12a). A similar southward shift of the ridge axis was seen during the 2007 Atlantic hurricane season, which also featured a strong positive IOD (Bell et al. 2008). Third, the anomalous southerly flow in the lower atmosphere was confined to the southern MDR and Gulf of Guinea region, rather than extending well into the central MDR and the African Sahel region (Fig. 4.11a).

The positive IOD also appears to have affected the La Niña-related convection patterns. One component of La Niña is an extensive area of enhanced convection across Indonesia and the eastern Indian Ocean. However, convection was suppressed over the eastern

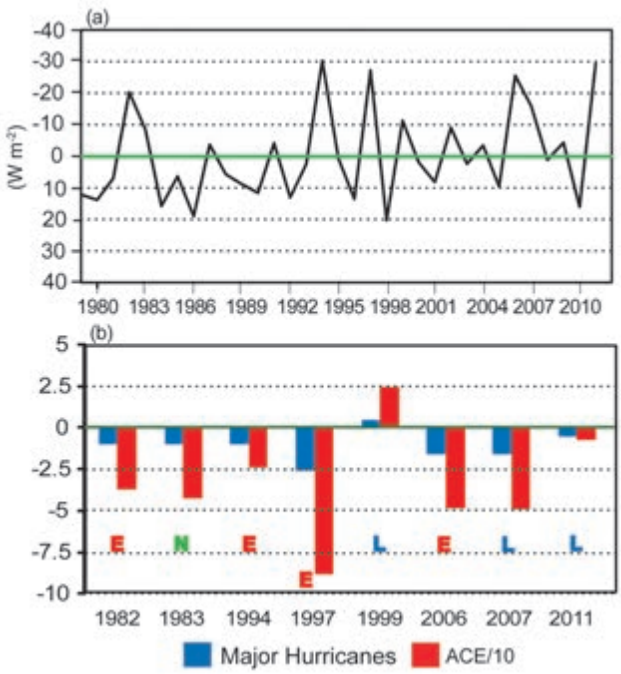

Fig. 4.17. (a) ASO time series of the IOD, calculated as the difference in area-averaged OLR anomalies (W m^{-2}) between the western and eastern Indian Ocean (western minus eastern; boxes shown in Fig. 4.14). Anomalies are with respect to the 1981–2010 base period. (b) Anomalous Atlantic major hurricane (blue) and ACE/10 (i.e., $\times$ 10^3 kt^2) activity associated with storms first named in the MDR when there was a strong positive IOD during ASO. Anomalies for years during 1979–1994 (low-activity era) and 1995–2011 (high-activity era) are based on the respective period means. Corresponding El Niño (red E), La Niña (blue L), and ENSO-neutral (green N) periods are indicated.

Indian Ocean during ASO 2011 in association with the positive IOD (Fig. 4.15), meaning that the La Niña forcing onto the atmospheric circulation was weaker than if no IOD signal had been present. A similar observation was made by Bell et al. (2008) for the 2007 Atlantic hurricane season.

3) Eastern North Pacific basin—M. C. Kruk, C. J. Schreck, and P. A. Hennon

(i) Seasonal activity

The Eastern North Pacific (ENP) basin is officially split into two separate regions for the issuance of warnings and advisories by NOAA's National Weather Service. NOAA's National Hurricane Center (NHC) is responsible for issuing warnings in the eastern part of the basin that extends from the Pacific Coast of North America to 140°W, while NOAA's Central Pacific Hurricane Center (CPHC) in Honolulu, Hawaii, is responsible for issuing warnings in the Central North Pacific region between 140°W and the date line. In this section, analysis summarizing the tropical cyclone (TC) activity in both these warning areas will be presented using combined statistics, along with information specifically addressing the observed activity and impacts in the Central North Pacific (CNP) region.

The ENP hurricane season officially spans from 15 May to 30 November, although storms can develop outside of the official season, especially during El Niño events. Hurricane and TC activity in the eastern area of the basin typically peaks in September, while in the central Pacific TC activity normally reaches its seasonal peak in August (Blake et al. 2009).

Only 11 named storms (NSs) formed in the ENP during 2011 and none formed in the CNP (Fig. 4.17). The 1981–2010 IBTrACS seasonal averages for the basin are 16.7 NSs, 8.9 hurricanes, and 4.3 major hurricanes. While the 2011 numbers are below average, all but one of the NSs (TS Fernanda) strengthened to at least hurricane status. The number of resulting hurricanes (10) and major hurricanes (6) were actually both above average. Five of the six major hurricanes even reached Category 4 status. This was the first time since records began in 1949 that more than 90% of the NSs became hurricanes and more than 50% also became major hurricanes. Despite the large fraction of strong storms, the ACE index for 2011 was 121.8×10^4 kt^2 (Fig. 4.18), which is below the 1981–2010 mean of 144.0×10^4 kt^2 (Bell et al. 2000; Bell and Chelliah 2006).

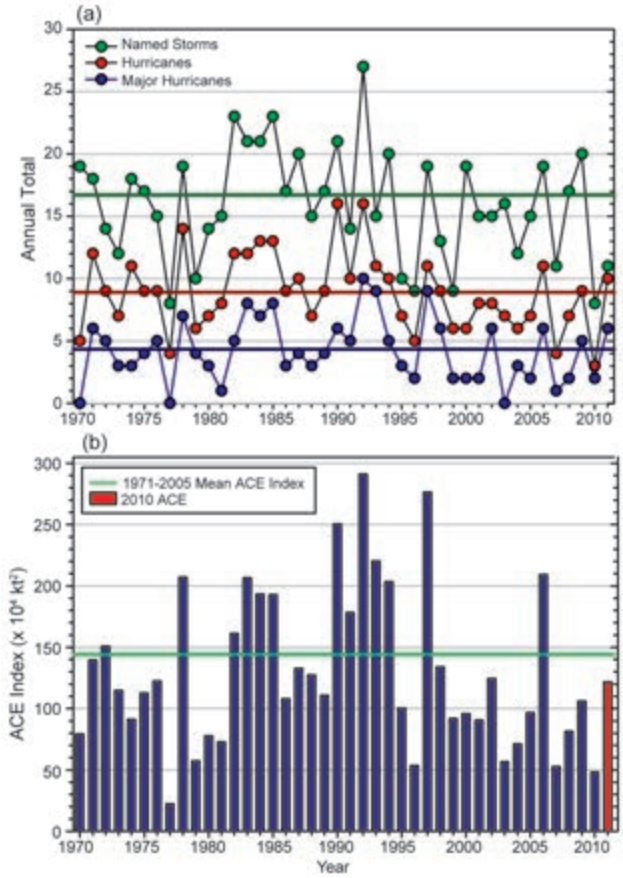

Fig. 4.18. Seasonal TC statistics for the ENP basin over the period 1970–2011: (a) number of named storms, hurricanes, and major hurricanes, and (b) the ACE index with the seasonal total of 2011 highlighted in red. The time series shown includes the corresponding 1981–2010 base period means for each parameter.

(ii) Environmental influences on the 2011 season

Figure 4.19 illustrates the background conditions for TC activity in the ENP during 2011. The overall patterns were dominated by La Niña. Sea surface temperatures (SSTs) were below normal over most of the ENP (Fig. 4.19a) and positive outgoing longwave radiation (OLR) anomalies (Fig. 4.19b, warm colors) suggest that convection was suppressed in the ITCZ. Enhanced vertical wind shear existed over most of the basin (Fig. 4.19c). Each of these factors acted to suppress TC activity, particularly in the ITCZ. Conditions were somewhat more favorable along the Central American coastline. Enhanced convection was observed along the coast (Fig. 4.19b, cool colors) and the SST anomalies were less negative in that area. Consistent with these patterns, most of the TCs did form near the coast.

Although conditions over the ENP were generally unfavorable for TCs during 2011, Fig. 4.19d shows 850-hPa westerly wind anomalies over the basin.

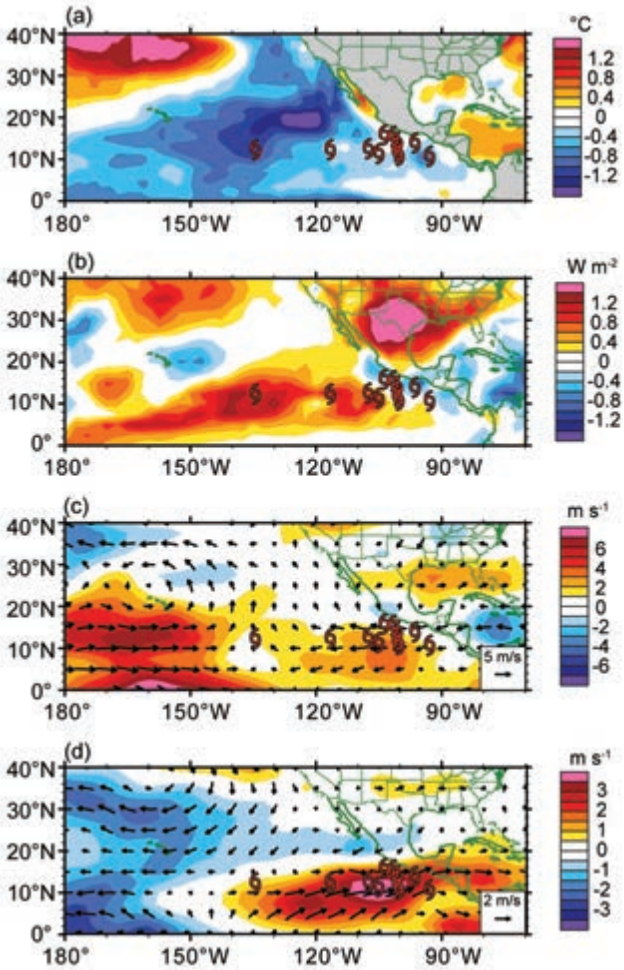

Fig. 4.19. Maps of Jun–Nov 2011 anomalies of (a) SST, (b) OLR, (c) 850-hPa–200-hPa vertical wind shear vector (arrows) and scalar (shading) anomalies, and (d) 850-hPa winds (arrows) and zonal wind (shading) anomalies. Anomalies are relative to the annual cycle from 1981–2010, except for SST, which is relative to 1982–2010 due to data availability. Hurricane symbols denote where each ENP TC attained TS strength. Wind data are obtained from the NCEP–DOE Reanalysis 2.

These anomalies favored TC genesis by enhancing the low-level cyclonic vorticity. The westerlies would also enhance easterly wave activity through barotropic energy conversion and wave accumulation (Maloney and Hartmann 2001; Aiyyer and Molinari 2008).

Eastern North Pacific TC activity is strongly influenced by the Madden-Julian oscillation (MJO; Maloney and Hartmann 2001; Aiyyer and Molinari 2008). Figure 4.20 shows the evolution of unfiltered (shading) and MJO-filtered (contours) OLR during the 2011 ENP hurricane season. The MJO filter contains eastward propagation with wave numbers 0–9 and periods of 30–96 days following Kiladis et al. (2005). While convection was generally suppressed over the ENP (Fig. 4.19b), Fig. 4.20 shows periods of enhanced convection (negative OLR anomalies) associated with the MJO. The TCs generally formed during these convective periods. Irwin, Jova, and Tropical Depression Twelve (not shown) developed in association with a particularly strong MJO during October 2011 (Fig. 4.20). The Wheeler and Hendon (2004) Real-time Multivariate MJO (RMM) Index shows a record value of 3.63 standard deviation amplitude during this event (M. C. Wheeler, 2011, personal communication).

(iii) TC impacts

Just one TC made landfall along the Pacific coast of Mexico during the season (Major Hurricane Jova). Two other TCs made a close brush against the shoreline, but never came ashore. In comparison with climatology, the 2011 season is near the 1951–2000 average of 1.34 landfalling TCs (Jáuregui 2003).

Along the Pacific coast of Mexico, Hurricane Beatriz (19–22 June) made a close approach to land from Acapulco northward to Manzanillo, causing some flooding and the closure of many popular tourist hotels. The rainfall was welcome, however, as it helped alleviate an ongoing severe drought across

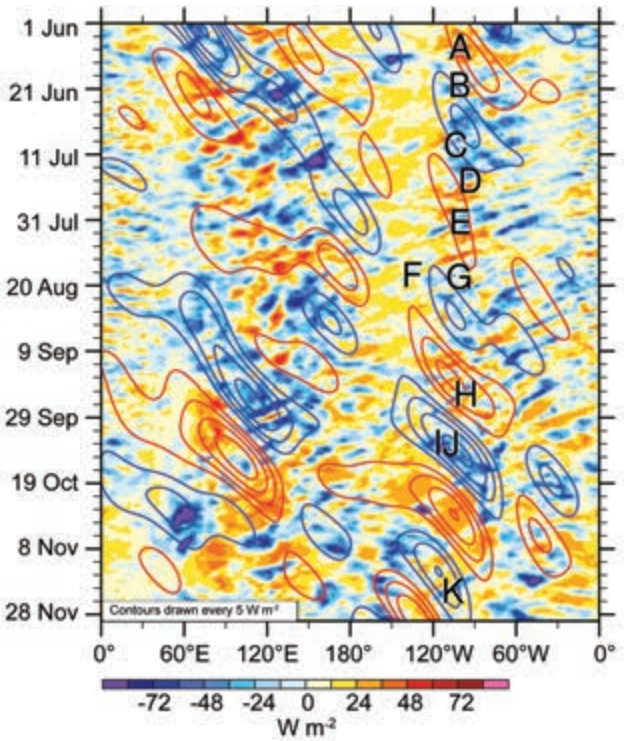

Fig. 4.20. Longitude–time Hovmöller of unfiltered (shading) and MJO-filtered (contours) anomalies of OLR averaged 10°N–20°N. Negative contours are drawn in blue, positive in red, and the zero contour is omitted. Letters indicate the genesis of ENP TCs.

the region. Beatriz eventually turned west and then southwest on 22 June and dissipated over the cooler waters of the open ocean.

The strongest storm of the season in the ENP was Major Hurricane Dora, which attained 135 kt (69 m s^{-1}) winds and a minimum central pressure of 929 hPa on 21 July. Just two days later the storm had weakened to tropical storm strength over the open waters of the eastern Pacific. The hurricane was impressively large and had a well-defined eye during its most intense phase. The only impacts to Mexico were high seas, dangerous rip currents, and a few rain showers along the south shores near Acapulco.

Major Hurricane Hilary (21–30 September) was a powerful Category 4 hurricane with peak wind speeds of 125 kt (64 m s^{-1}). This storm peaked in intensity very close to the Mexican coastline, but never made landfall. The impacts from Hilary were focused near Tabasco, Mexico, where more than 210 mm of rain was attributed to spiral bands around the storm. Low-lying agricultural fields were plagued by the rains, forcing some farmers to evacuate their livestock.

Jova (6–13 October) was the most damaging storm of the season and was blamed for eight deaths and six injuries as it made landfall near Jalisco, Mexico, as a Category 2 hurricane. Rainfall from Jova was estimated at over 250 mm, which left the key city streets and port of Manzanillo under 1–2 meters of standing water.

Kenneth was the strongest recorded late-season major hurricane (19–25 November) in the ENP basin, with peak winds at 125 kt (64 m s^{-1}). The storm's track was nearly due west along the 10° N line of latitude. Despite its strength, no major impacts were reported because it stayed far from land.

4) Western North Pacific basin—S. J. Camargo

The tropical cyclone (TC) data used here is from the Joint Typhoon Warning Center (JTWC) Western North Pacific (WNP) best-track dataset for the 1945–2010 period and from the JTWC preliminary operational data for 2011. The 1981–2010 IBTrACS seasonal averages for the basin are 25.4 (total systems), 15.5 (typhoons), and 6.0 (super typhoons). The total number of TCs in the season was 27, with 20 named storms (TSs), 10 typhoons (TYs), and 4 super typhoons (STYs). Furthermore, a tropical depression (TD) was named as Tokage by the Regional Specialized Meteorological Center (RSMC)-Tokyo, but was not assessed as a named storm by the JTWC. In Fig. 4.21a, the number of named storms, typhoons, and super typhoons per year is shown for the period 1945–2011 (based on JTWC data).

The 2011 WNP TC season started in April with two TDs (1W and 2W), followed by Tropical Storm Aere in early May. At the end of May, Super Typhoon Songda occurred. In June, three TSs formed in the WNP (Sarika, Haima, and Meari), but none intensified into a typhoon. From the four TCs that formed in July, one was a TD (Tokage) and three became typhoons (Ma- On, Nock-ten, Muifa), with Muifa reaching super typhoon status. Another super typhoon occurred at the end of August (Nanmadol), which was preceded by Typhoon Merbok and TD 13W, with Tropical Storm Talas forming a few days after Super Typhoon Nanmadol. Seven TSs occurred during September, the highest monthly number of the season, tying the maximum number of September NSs in the historical record (Fig. 4.21c). Of these seven TCs, four became typhoons (Roke, Sonca, Nesat, and Nalgae), with Nalgae becoming the fourth super typhoon of the 2011 season. In contrast, October was quiet, with only one TS forming in the WNP (Fig. 4.21c), an unusual event, which has only happened during three previous years of the historical record (1945, 1946, and 1976). Low TC activity continued in November, when only two TDs developed (24W and 25W; Figs. 4.21c,e). Only three other years in the historical record had no named storms during November (1963, 1994, and 2010). The season finished with TD 26W and TS Washi forming during December.

The total accumulated cyclone energy (ACE) in the 2011 season was below normal, in the bottom quartile of the climatological distribution (Fig. 4.22a). Due to the occurrence of Super Typhoon Songda, the value of ACE for the month of May was in the top quartile of the climatological distribution (Fig. 4.22b). Songda was responsible for 88% of the May ACE. July and August ACE values were also above the climatological median for those months, due mainly to Super Typhoons Muifa and Nanmadol. September ACE was slightly below the climatological median, even with the presence of Super Typhoon Nalgae. The ACE in October was in the bottom 10th percentile of the climatological distribution, while the ACE value in November was zero, which occurred previously only in 1963 and 2010. The highest value of ACE for a single TC in 2011 was Super Typhoon Muifa (top fifth percentile of the climatological and historical distributions), followed by Super Typhoon Songda, Typhoon Ma-on, and Super Typhoon Nanmadol, all in the top quartile of the climatological and historical distributions of ACE for individual storms.

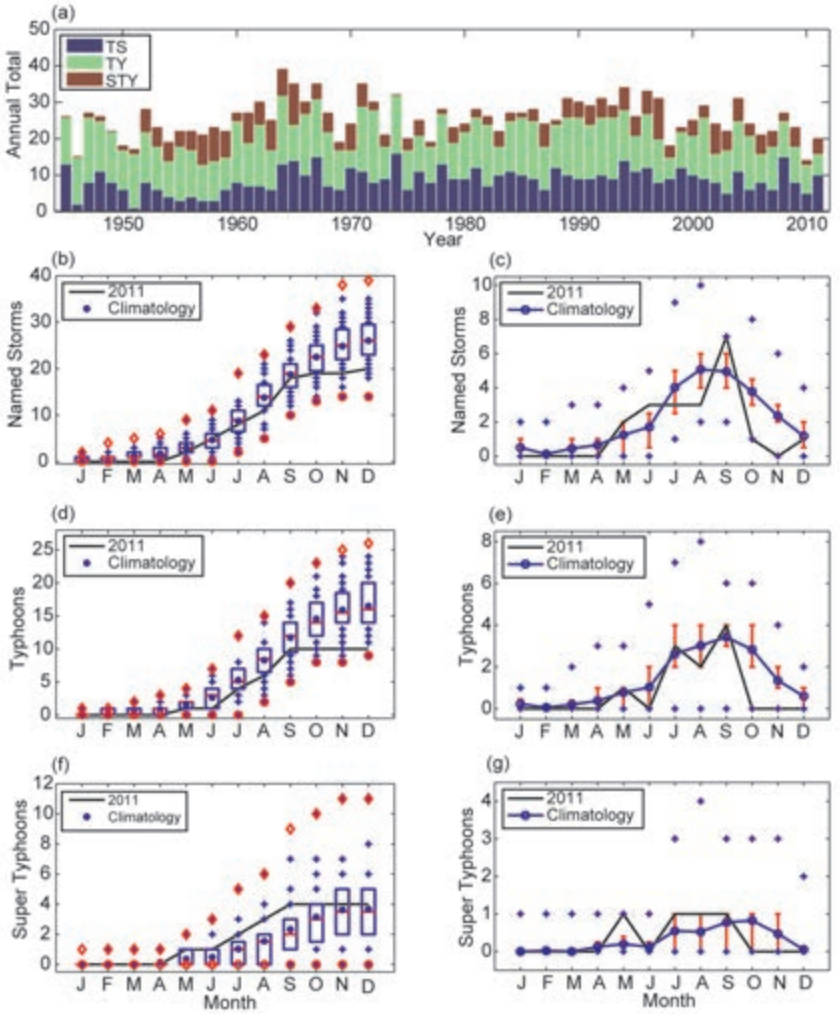

Fig. 4.21. (a) Number of TSs, TYs, and STYs per year in the WNP for the period 1945–2011. Panels (b), (d), and (f) show the cumulative number of tropical cyclones with TS intensity or higher (named storms), TYs, and STYs, respectively, per month: 2011 (black line), and climatology (1971–2010) as box plots (interquartile range: box; median: red line; mean: blue asterisk; values in the top or bottom quartile: blue crosses; high (low) records in the 1945–2010 base period: red diamonds/circles). Panels (c), (e), and (g) show the number of NSs, TYs, and STYs, respectively, per month in 2011 (black line) and the climatological mean (blue line); the blue "+" signs denote the maximum and minimum monthly historical records; and the red error bars show the climatological interquartile range for each month (in the case of no error bars, the upper and/or lower percentiles coincide with the median). (Source: 1945–2010 JTWC best-track dataset and 2011 JTWC preliminary operational track data)

There were 124 days with TCs and 109.5 days with TSs in 2011 in the WNP, both in the bottom quartile of the climatological distribution (climatological medians: 157.25 and 134.5 days, respectively). From these active days, only 78.5 had TYs, also in the bottom quartile of the climatological distribution (climatological median 117.75 days). There were 14.5 days with intense typhoons (Categories 3–5), below the climatological median of 20 days. In 2011 the number of TC days with TYs and intense TYs were 63% and 12%, respectively (climatological average is 74% and 12%). The median lifetime for TSs and TYs in 2011 was 6.87 days, below the median climatology of 8 days. From the 20 TSs and TYs, 2 (5) had a lifetime in the top (bottom) quartile of the distribution (25th percentile: 5.75 days; 75th percentile: 10.75 days). The storms with the longest lifetimes in 2011 were Super Typhoon Muifa (14.25 days) and Typhoon Ma-on (13.25 days).

The mean genesis location in 2011 was 14.9°N, 137.6°E, which was shifted northwestward of the climatological mean genesis position (13.1°N, 142.8°E). The mean track position (21.4°N, 129.8°E), was also shifted northwestward of the mean climatological track position (19.4°N, 133.7°E). This northwestward shift is typical of La Niña years (Camargo et al. 2007; Chan 2000; Lander 1994). The 2010/11 moderate La Niña event weakened considerably during the 2011 Northern Hemisphere spring and summer months, returning in the Northern Hemisphere fall as a weak-to-moderate La Niña, influencing the genesis and track positions of the typhoons in the 2011 season. There were 13 storms that made landfall in 2011, slightly below the JTWC 1951–2010 climatological median of 15. Two systems made landfall as TDs (median is three), eight made landfall as TSs (median is six), and two struck as TYs (median is four).

One of the remarkable features of the 2011 season was the dramatic change in western North Pacific TC activity from September (tying the historical maximum for that month) to October (tying the historical

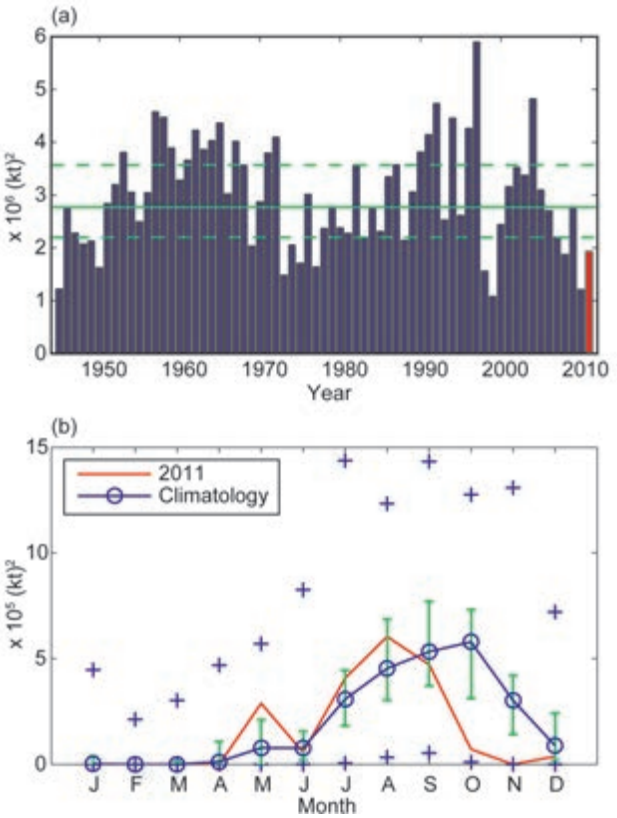

Fig. 4.22. (a) ACE index per year in the WNP for 1945–2011. The solid green line indicates the median for the climatology years 1971–2010, and the dashed lines show the climatological 25th and 75th percentiles. (b) ACE index per month in 2011 (red line) and the median during 1971–2010 (blue line), where the green error bars indicate the 25th and 75th percentiles. In case of no error bars, the upper and/or lower percentiles coincide with the median. The blue "+" signs denote the maximum and minimum values during the period 1945–2011. (Source: 1945–2010 JTWC best-track dataset, 2011 JTWC preliminary operational track data)

minimum for that month). The reason for this abrupt change appears to be a combination of two factors: the strengthening of the La Niña event and an MJO event in the suppressed phase in October over the western North Pacific. Figure 4.23 shows the environmental conditions in the July–September (JAS) season (left panels) and the October–December (OND) season (right panels) over the western North Pacific. In Fig. 4.23, the anomalies of the potential intensity (Emanuel 1988, 1995; Figs. 4.23a,b), genesis potential index (GPI; Camargo et al. 2007; Figs. 4.23c,d) and 600-hPa relative humidity (Figs. 4.23e,f) are shown in the top, middle, and bottom panels, respectively. The potential intensity positive anomalies are dominant in OND. In contrast, the positive anomalies of GPI in OND occur only in a small region near the Philippines and very near the equator, in agreement with the low occurrence of TCs in OND. While neither the JAS nor the OND GPI has the typical La Niña pattern, with positive anomalies in the northeast and negative anomalies in the southwestern part of the basin, the OND GPI is more similar to other La Niña events, confirming that the cold event only affected the TC activity in the later part of the season. The relative humidity anomalies are dominantly below normal in OND in the region, which appears to be the main reason for the negative anomalies in GPI in OND, similar to other La Niña events (Camargo et al. 2007).

The largest impacts of the 2011 season occurred due to a late-season storm in December. Tropical Storm Washi (named Sendong in the Philippines) first made landfall in the island of Mindanao in the Philippines on 16 December, then made a second landfall over the island of Palawan (Philippines) the next day. Though the Philippines are often struck by tropical cyclones, the storms usually take a more northern path, affecting the island of Luzon and rarely make landfall in Mindanao. Lyon and Camargo (2009) have shown that during La Niña events, there is a tendency to have below-normal rainfall in Philippines during JAS (mainly in northern Philippines), while during OND there is above-normal rainfall in the whole Philippines, including Mindanao, and that these rainfall anomalies can be related to TCs affecting the Philippines. The flash flooding caused by Washi in Mindanao was catastrophic, with more than 1250 deaths. The storm was unusually wet. Torrential rain fell over a period of 10 hours, bringing more than 200 mm in some places, destroying some villages with flood waters and landslides (see http://www.mb.com.ph/articles/345284/pagasa-typhoons-142mm-rain-12-hours-super-heavy). On 17 December, more than 100 000 people were evacuated. The economic damage in infrastructure and agriculture in the region was also very high.

5) Indian Ocean basins

(i) North Indian Ocean—M. C. Kruk and K. L. Gleason

The North Indian Ocean (NIO) tropical cyclone (TC) season typically extends from April to December, with two peaks in activity during May–June and November, when the monsoon trough is positioned over tropical waters in the basin. TCs in the NIO basin normally develop over the Arabian Sea and Bay of Bengal between latitudes 8°N and 15°N. These systems are usually short lived and relatively weak and often quickly move into the Indian subcontinent. However, strong and "severe cyclonic storms"

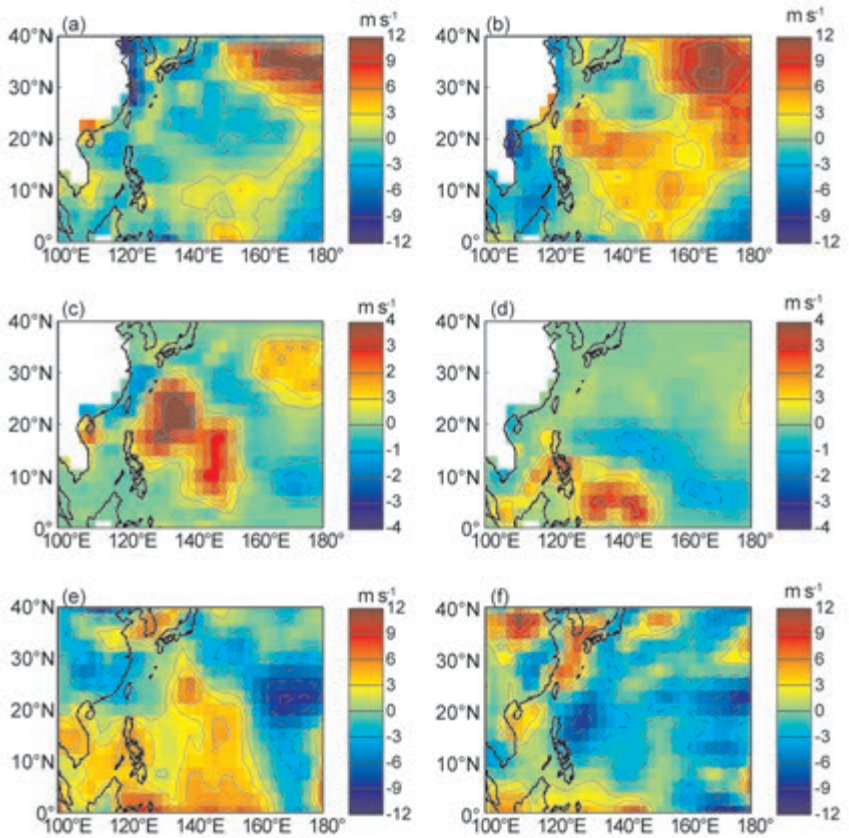

Fig. 4.23. Potential intensity anomalies (m s^{-1}) for (a) JAS and (b) OND 2011 from 1971–2010 climatology. Genesis potential index anomalies for (c) JAS and (d) OND 2011. 600-hPa relative humidity anomalies (in %) for (e) JAS and (f) OND 2011. In all panels, positive contours are shown in solid lines, negative contours in dash dotted lines and the zero contour in a dotted line. [Source: atmospheric variables: NCEP/NCAR Reanalysis data (Kalnay et al. 1996); SST (Smith and Reynolds 2005).]

can develop with winds exceeding 130 kt (67 m s^{-1}; Neumann et al. 1993).

The 2011 TC season produced six named storms (NSs), one cyclone (CYC), and no major cyclones (MCYC; Fig. 4.24a). While the number of NSs is slightly above the 1981–2010 IBTrACS seasonal average of 4.0 NSs, the numbers of CYCs and MCYCs are below the long-term averages of 1.4 and 0.6, respectively. The season produced an ACE index value of 12.4×10^4 kt^2, which is below the 1981–2010 average of 16.2×10^4 kt^2 (Fig. 4.24b). There is generally an enhancement in tropical cyclone activity, especially in the Bay of Bengal, during the cool phase of ENSO (Singh et al. 2000), which was the prevailing condition for that season. The strongest storm of the year, Cyclone Thane, developed in the Bay of Bengal late in the season.

The first three storms of the season (Tropical Storms One, Two, and Keila) formed close to land and remained relatively weak as they came ashore. The major impact from these systems was heavy rainfall. All storms weakened below tropical storm strength within about 12 hours of being named as they interacted with land and gradually dissipated.

Tropical Storm Two (19–20 October) was the most damaging storm of the year, despite having peak winds of only 35 kt (18 m s^{-1}). The storm formed off the coast near the border of Bangladesh and Myanmar and slowly moved ashore. Early estimates indicate that over 200 people died from the storm and economic damages exceeded $1.5 million (US dollars). The storm caused massive flash flooding, washed away over 2000 homes and left many stranded in high water for days after the storm (http://thewatchers.adorraeli.com/2011/10/21/myanmar-battered-with-flash-floods-and-tropical-cyclone).

In the Arabian Sea, Tropical Storm Keila (1–3 November) caused havoc and damages in Muscat, Oman, as it made landfall on 2 November. Widespread heavy rains flooded city streets, forced the evacuation and closure of hospitals, and resulted in 14 deaths and 200 injuries (http://earthobservatory.nasa.gov/NaturalHazards/view.php?id=76346). The last storm to hit the Muscat region was in May 2002.

The strongest storm of the year, Cyclone Thane (Fig 4.25), occurred very late in the season (25–30 December). The storm developed as a tropical disturbance within the monsoon trough in the Bay of Bengal and intensified into a cyclone west of Indonesia with maximum sustained winds of 80 kt (40 m s^{-1}). The storm made landfall on 30 December near Tamil Nadu and Andhra Pradesh in India as a weakening very severe cyclonic storm. Damages and injuries from the storm in Andhra Pradesh were minimized by good planning and preparation, as well as adequate logistics and supplies in place. However, in Tamil Nadu, closer to where the storm made landfall, some cities were completely cut off as

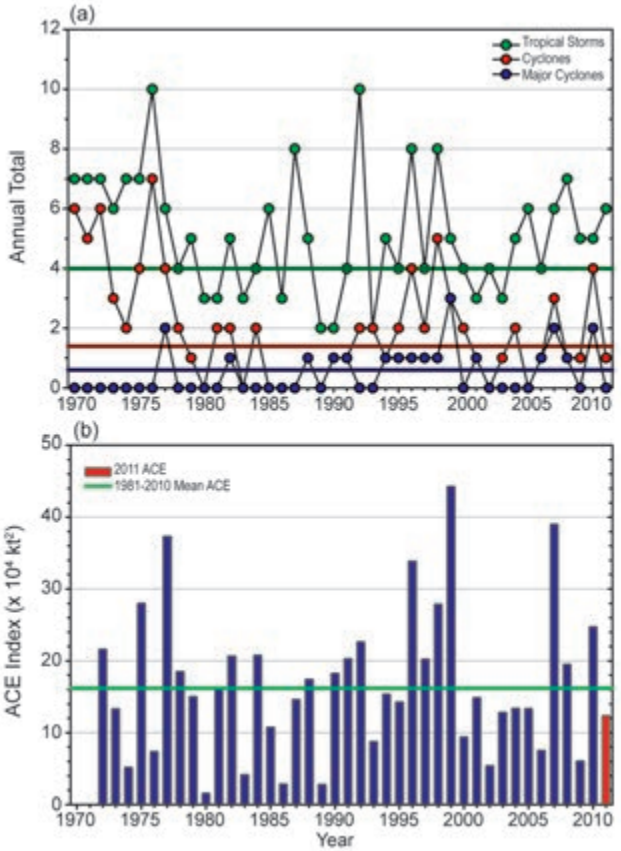

Fig. 4.24. Annual TC statistics for the NIO over the period 1970–2011: (a) number of tropical storms, cyclones, and major cyclones, and (b) the estimated annual ACE Index ($kt^2 \times 10^4$) for all tropical cyclones during which they were at least tropical storm or greater intensities (Bell et al. 2000). The 1981–2010 base period means are included in both (a) and (b). Note that the ACE Index is estimated due to a lack of consistent six-hour-sustained winds for every storm.

interior road networks were damaged and washed away. Nearly three dozen fatalities are blamed on the storm in Cuddalore, India (http://www.disasterwatch.net/resources/NeedAssessment-Thanecylone.pdf).

(ii) South Indian Ocean—K. L. Gleason and M. C. Kruk

The South Indian Ocean (SIO) basin extends south of the equator from the African coastline to 105°E, with most cyclones (CYCs) developing south of 10°S. The SIO tropical cyclone (TC) season extends from July to June encompassing equal portions of two calendar years (e.g., the 2010/11 season is comprised of storms from July 2010 to June 2011). The peak activity typically occurs from December to April when the ITCZ is located in the Southern Hemisphere and is migrating toward the equator. Historically, the vast majority of the landfalling CYCs in the SIO impact Madagascar, Mozambique, and the Mascarene Islands, including Mauritius and Réunion.

The historical SIO TC data is probably the least reliable of all the TC basins (Atkinson 1971; Neumann et al. 1993), primarily due to a lack of historical record keeping by individual countries and no centralized monitoring agency; however, the historical dataset for the region has been updated (Knapp et al. 2010). The historical data are noticeably deficient before reliable satellite data were operationally implemented in the region beginning about 1983.

The 2010/11 SIO season storm numbers were below average, with six named storms (NSs), two CYCs, and one major cyclone (MCYC; Fig. 4.26a). The 1981–2010 IBTrACS seasonal averages are 12.5 NSs, 6.1 CYCs, and 2.1 MCYCs. The quiet season is also reflected in the 2010/11 ACE index of 27.5×10^4 kt^2, which was below the 1981–2010 average of 91.5 $\times 10^4$ kt^2 (Fig. 4.26b). This is the third consecutive year with below-normal ACE values, and the lowest since 1983.

The strongest cyclone and the only one to make landfall during the 2010/11 season was Major Cyclone Bingiza. On 8 February, an area of convection developed approximately 880 km north-northeast of

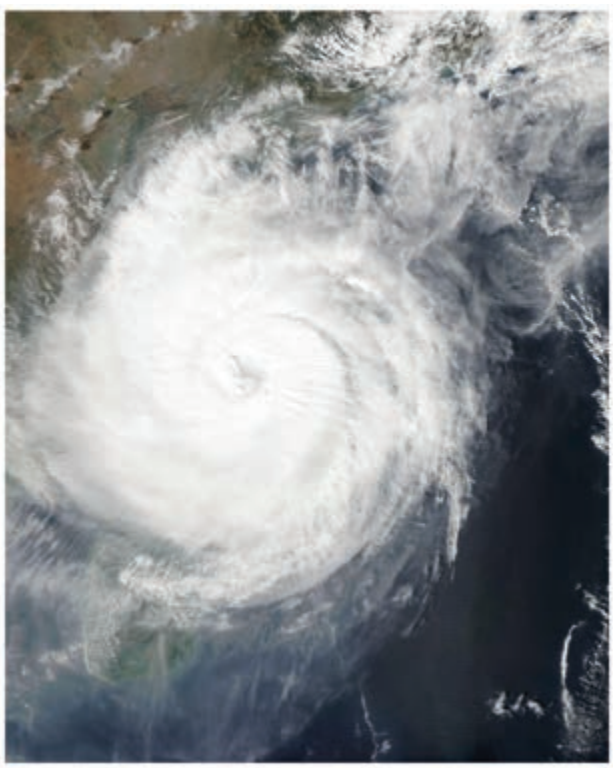

Fig. 4.25. Satellite image of Cyclone Thane over the NIO at the apex of its strength prior to landfall. (Source: NASA Earth Observatory, AQUA MODIS satellite imagery)

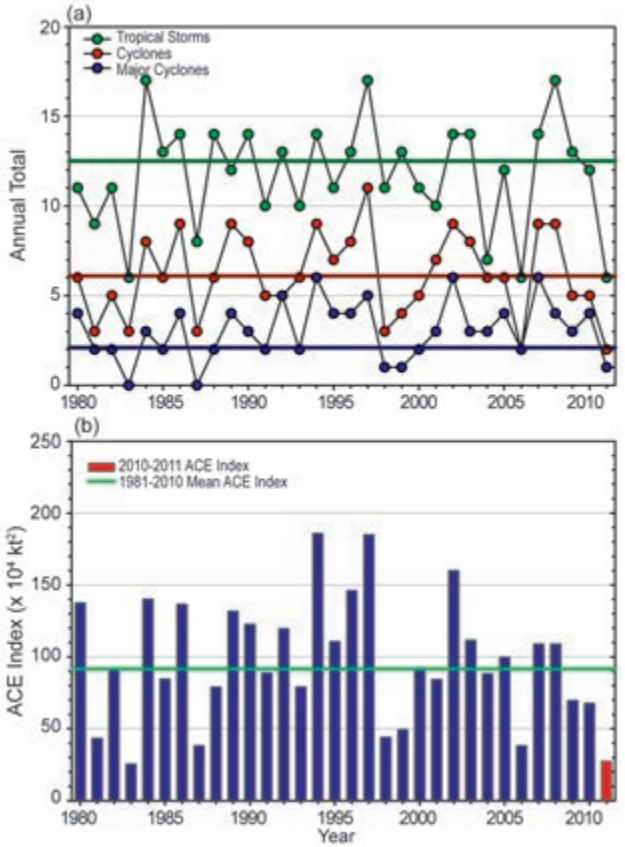

Fig. 4.26. Annual TC statistics for the SIO over the period of 1970–2011: (a) number of tropical storms, cyclones, and major cyclones and (b) the estimated annual ACE Index ($kt^2 \times 10^4$) for all tropical cyclones during which they were at least tropical storm or greater intensities (Bell et al. 2000). The 1981–2005 base period means are included in both (a) and (b). Note that the ACE Index is estimated due to a lack of consistent six-hour-sustained winds for every storm.

La Réunion Island. As this convection moved west-southwestward, the system gradually became more organized and was named Bingiza late on 9 February. A slow moving cyclone, Bingiza continued to migrate to the southwest and was upgraded to a severe tropical storm about 335 km east of the northeast coast of Madagascar on 12 February. Bingiza began to develop rapidly as it continued to move toward the Madagascar coast, reaching peak intensity on 13 February with maximum sustained winds of 89 knots (46 m s^{-1}) and a minimum pressure of 953 hPa, making it an intense tropical cyclone. On 14 February, Major Cyclone Bingiza made landfall near Saranambana, along Madagascar's northeastern coast, and quickly weakened over land. After Bingiza emerged over the Mozambique Channel between Africa and Madagascar on 15 February as a tropical depression, it reintensified into a tropical storm over the warm waters and made a second landfall along Madagascar's southwestern coast, producing five days of rainfall in a region already saturated by previous flooding events. The storm was responsible for 22 deaths and the destruction of 25 000 homes; a large portion of the food crops in several districts was destroyed as a result of the heavy wind and rains (http://reliefweb.int/node/392511).

6) Southwest Pacific basin—A. M. Lorrey, S. McGree, J. A. Renwick, and S. Hugony

The 2010/11 TC season for the southwest Pacific (between 135°E and 120°W) started up in late December with the formation of Tropical Cyclone Tasha and concluded in late March with Tropical Cyclone Bune. A total of nine TCs occurred in the region, which was consistent with the number of predicted storms based on the Island Climate Update analog forecast (see http://www.niwa.co.nz/climate/icu). Five TCs reached at least Category 3 on the Saffir-Simpson scale, and three systems reached at least Category 4. This activity was also in line with the prediction of at least three storms reaching Category 3 status and at least one storm reaching Category 4 strength. There were more numerous TCs during the early part of the season—the peak activity occurred in January, which had five named storms. Several tropical depressions also formed late in the season; however, none developed into a named storm. Damages associated with TC activity for the 2010/11 season are estimated to have exceeded at least $3.5B (US dollars), with a total of four reported fatalities. Forecasts indicated an increased risk of TCs impacting island nations surrounding the Coral Sea and to the southwest of Fiji. New Zealand was also at higher risk of experiencing an extratropical cyclone interaction this season.

The distribution of TC activity was in line with expectations, with six extratropical cyclones (Sinclair 2002) entering the New Zealand sector (some having greater impacts than others). Australia (as noted in section 4d7) was significantly affected by the strongest event of the season when TC Yasi made landfall in Queensland on 3 February. Yasi is estimated to be the second costliest TC in Australian history. The 1981–2010 IBTrACS seasonal averages for the basin are 7.9 named storms, 7.7 TCs, and 4.3 major TCs.

7) Australian region basin—B. C. Trewin

(i) Seasonal activity

The 2010/11 tropical cyclone (TC) season was near normal in the broader Australian basin (areas south of the equator and between 90°E and 160°E[5], which includes Australian, Papua New Guinea, and Indonesian areas of responsibility). The season produced 11 TCs, near the 1983/84 – 2010/11 average (the average coincides with comprehensive satellite coverage of the region) of 10.8 and somewhat counter to the well-above-normal activity typical of strong La Niña seasons in the Australian region; the season was well-above average during the first half of the season, but only 1 TC formed after mid-February. There were no TCs in March for only the second time since the satellite era began around 1970. The 1981–2010 IBTrACS seasonal averages for the basin are 9.9 NSs, 7.5 TCs, and 4.0 major TCs.

There were four TCs in the eastern sector[6] of the Australian region during 2010/11 (one of these, Yasi, entered from the Southwest Pacific region), and seven TCs in the western sector (two of which, Carlos and Errol, formed in the northern sector, that sector's only TCs of the season). Four systems made landfall in Australia as TCs, while one was dissipating when it made landfall on the Indonesian portion of Timor.

(ii) Landfalling and other significant TCs

The most significant TC of the season was Yasi, the most intense TC to make landfall in Queensland since at least 1918. Yasi formed north of Vanuatu on 30 January and entered the Australian region late on 31 January. It continued to track west-southwest towards the Australian coast, passing directly over Willis Island on the morning of 2 February and reaching Category 5 intensity that afternoon (see http://www.bom.gov.au/cyclone/about/intensity.shtml for Australian tropical cyclone classification system).

Yasi made landfall on 3 February near Mission Beach, about halfway between Cairns and Townsville. At landfall it was near its peak intensity of 110 kt (57 m s^{-1}), and a pressure of 929 hPa was recorded by a barometer near Mission Beach. There was also a peak storm surge of 5.3 m near Cardwell, to the eye's south. There were heavy rains along Yasi's track, with a maximum 24-hour total of 471 mm at South Mission Beach. Yasi weakened steadily after landfall but remained a TC until it reached the Mount Isa area, while moisture from the TC contributed to flash flooding in South Australia and Victoria on 4–5 February. There was widespread and severe damage to property and vegetation from wind and storm surge, with Tully, Mission Beach, and Cardwell the worst-affected centers.

Two other TCs reached Category 4 intensity, but neither made landfall. Zelia tracked parallel to the east coast of Australia between 14 and 18 January, passing southwest of New Caledonia and just northeast of Norfolk Island towards the end of its life. Its peak intensity of 100 kt (51 m s^{-1}) was reached on 16 January near 19°S, 158°E, to the west of New Caledonia. Bianca formed on 26 January west of Broome, and then tracked parallel to the northwest coast, before moving farther offshore after passing north of Exmouth and reaching its peak intensity of 95 kt (49 m s^{-1}) near 25°S, 106°E. It then recurved southeast, resulting in a TC warning being issued for metropolitan Perth for the first time since 1989, but ultimately weakened below TC intensity before reaching the coast.

Carlos, which was an identifiable system from 13 to 26 February, only briefly reached Category 1 intensity near Darwin on 16 February. After tracking west-southwest across the Kimberley region, it reintensified after crossing out to sea near Broome, before returning to track along the coast between Karratha and Exmouth as a Category 2 system on 22–23 February. Carlos continued to move westward away from the coast on 24 February, reaching its peak intensity of 65 kt (33 m s^{-1}) as it did so, before dissipating off the coast on 26 February. The main impacts of Carlos arose from extremely heavy rain in the Darwin area as the system formed, with Darwin setting new records for one-day (367.6 mm), three-day (684.8 mm), seven-day (847.4 mm), and monthly (1110.2 mm) rainfall. Widespread flooding occurred through the region. A tornado associated with the TC also caused significant damage in Karratha.

The other two landfalls on the Australian mainland during the season were both in Queensland: Tasha made landfall just south of Cairns on 25 December as a Category 1 system [40 kt (21 m s^{-1})] and Anthony near Bowen on 30 January as a Category 2 system [50 kt (26 m s^{-1}) sustained winds]. Both made landfall near their peak intensity. Neither caused any major wind or storm surge damage but moisture

[5] The Australian Bureau of Meteorology's warning area overlaps both the southern Indian Ocean and Southwest Pacific.

[6] The eastern sector covers areas east of the eastern Australian coast to 160°E, as well as the eastern half of the Gulf of Carpentaria. The western sector covers areas between 90°E and 125°E. The northern sector covers areas from 125°E to the western half of the Gulf of Carpentaria.

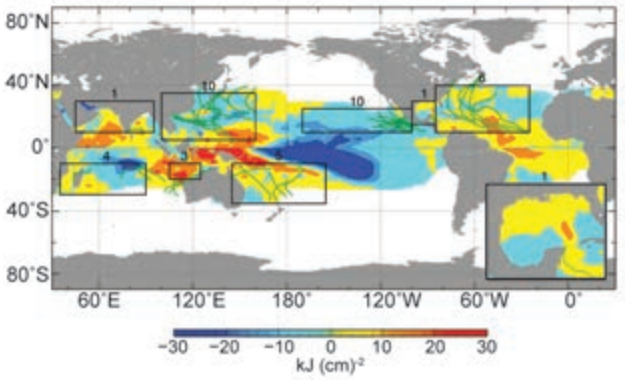

Fig. 4.27. Global anomalies of TCHP corresponding to 2011 computed as described in the text. The numbers above each box correspond to the number of Category 1 and above cyclones that traveled within each box. The Gulf of Mexico conditions during Jun–Nov 2011 are shown in the insert shown in the lower right corner.

from both, particularly Tasha, contributed to flooding farther inland. Errol, with a peak intensity of 65 kt (33 m s^{-1}), formed west of Darwin and moved to the northwest dissipating as it made landfall on the Indonesian island of Timor (not to be confused with the independent nation of East Timor) on 18 April.

e. *Tropical cyclone heat potential*—G. J. Goni, J. A. Knaff, and I-I Lin

This section summarizes the seven previously described TC basins from the standpoint of tropical cyclone heat potential (TCHP), by focusing on upper ocean temperature conditions during the season with respect to average values. TCHP, defined as the ocean heat content contained between the sea surface and the depth of the 26°C isotherm, has been shown to be more closely linked to intensity changes of tropical cyclones than sea surface temperature (SST) alone (Shay et al. 2000; Goni and Trinanes 2003; Lin et al. 2008, 2009a), provided that atmospheric conditions are also favorable. In general, fields of TCHP show high spatial and temporal variability associated with oceanic mesoscale features that can be globally detected with satellite altimetry (Lin et al. 2008; Goni et al. 2009). It has been shown that areas with high values of TCHP can be an important factor for the rapid intensification of tropical cyclones (TCs; e.g., Shay et al. 2000; Mainelli et al. 2008; Lin et al. 2009a).

To examine TCHP interannual variability, anomalies are computed during the months of TC activity in each hemisphere: June through November in the Northern Hemisphere and November through April in the Southern Hemisphere. Anomalies are defined as departures from the mean TCHP calculated during the same months for the period 1993–2011. These anomalies show large variability within and among the tropical cyclone basins. During the 2011 season, the basins exhibited the following TCHP anomalies:

- The Western North Pacific (WNP) basin exhibited both positive and negative TCHP anomaly values, while the Eastern North Pacific (ENP) had slightly negative values (Fig. 4.27).
- The Southwest Pacific basin had both positive and negative anomalies, although the cyclone basin continued exhibiting mostly high positive values.
- In the North Indian Ocean (NIO) basin, both the Bay of Bengal and Arabian Sea exhibited positive anomalies.
- In the Atlantic basin, the Gulf of Mexico (Fig. 4.27 insert, lower right) showed positive and negative anomalies associated with the variability of the Loop Current. In contrast to 2009 and 2010, the tropical Atlantic exhibited mostly negative values, which were largely observed in the sea height and sea surface temperature fields[7].
- In general, with respect to the 2010 anomalies, the WNP and NIO basins exhibited lower values of TCHP. On the other hand, the SIO and Southwest Pacific basins, as well as sections of the Gulf of Mexico, showed elevated TCHP values (Fig. 4.28).

[7] It should be noted that there were warm SST anomalies in the Atlantic in 2011, and SSTs do not necessarily equate to TCHP values.

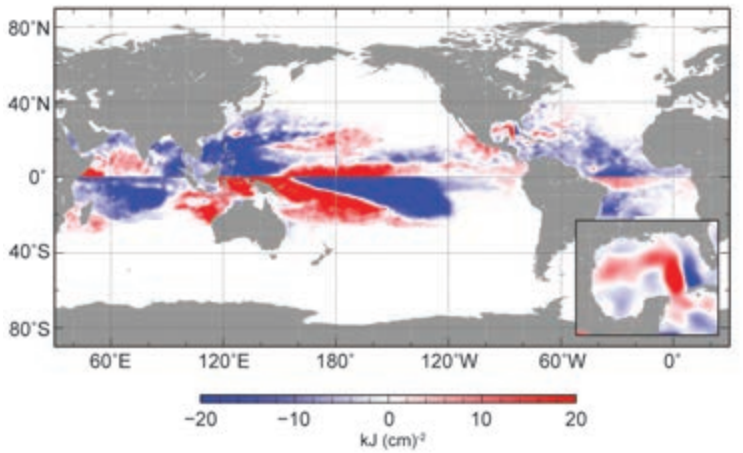

Fig. 4.28. Differences between the TCHP fields in 2011 and 2010.

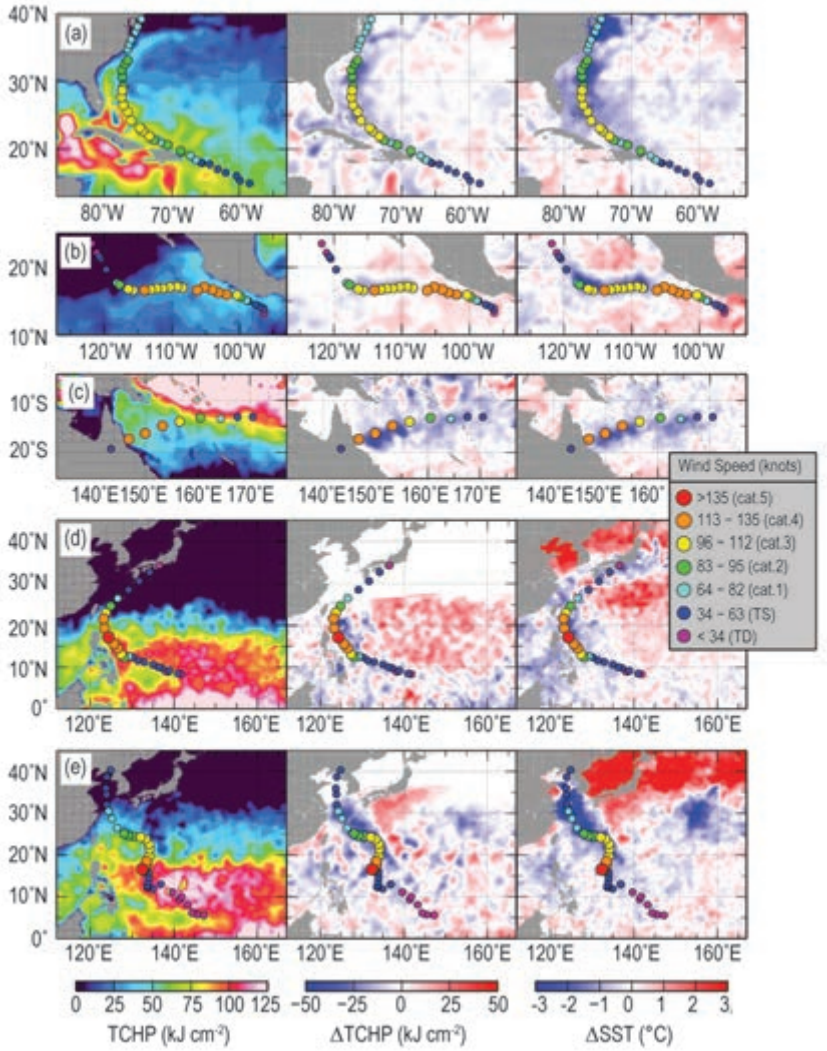

Fig. 4.29. (left) Oceanic TCHP and surface cooling given by the difference between post- and pre-storm values of (center) TCHP and (right) SST for Hurricanes (a) Irene and (b) Hilary, (c) Tropical Cyclone Yasi, and Typhoons (d) Songda and (e) Muifa. The TCHP values correspond to two days before each TC reaches its maximum intensity value.

Five TCs, where the location of their intensification coincided with relatively high values of TCHP along their tracks, are highlighted in Fig. 4.29. These were Irene (Atlantic), Hilary (ENP), Yasi (Southwest Pacific), and Songda and Muifa (WNP). The cooling associated with the wake of major TCs reached values of up to 50 kJ cm^{-2} in TCHP and above 3°C in SST. This is important since large cooling could affect the intensification for subsequent TCs in the same region and may also influence the upper ocean thermal structure on regional scales within weeks to months after the passage of the cyclones (Emanuel 2001; Hart et al. 2007; Dare and McBride 2011).

Hurricane Irene, the first hurricane of the Atlantic season, developed during late August, and rapidly became a Category 3 major hurricane (Fig. 4.29a), when traveling over waters with TCHP values above 60 kJ cm^{-2}, and the cooling produced by this TC, even after weakening, reached values larger than 3°C in its track.

In the case of ENP Hurricane Hilary, while moving roughly parallel to the Mexican coast and within a very favorable atmospheric environment, Hilary quickly intensified up to 55 kts (28 m s^{-1}) on 22 September. While still moving west-northwest within a similarly favorable atmospheric environment, Hilary encountered higher values of TCHP and became a hurricane (Fig. 4.29b). The TCHP increased nearly three-fold from 15 kJ cm^{-2} to values exceeding 40 kJ cm^{-2} as the TC began its most rapid period of intensification. In this case, TCHP fields improved operational forecasts that were made by both the Statistical Hurricane Intensity Prediction Scheme (SHIPS; DeMaria et al. 2005) and Rapid Intensity Index (RII; Kaplan et al. 2010). During the next 24 hours, Hilary intensified very rapidly from 55 kts to 125 kts (28 m s^{-1} to 64 m s^{-1}). It is noteworthy that the atmospheric conditions remained nearly constant during this period, illustrating the positive effect that TCHP has on TC development and demonstrating how TCHP information can improve TC intensity forecast model output. With respect to Hurricane Hilary for example, TCHP values remained greater than 30 kJ cm^{-2} and this, coupled with favorable atmospheric conditions, persisted for the next 48 hours, allowing Hilary to sustain itself as a major hurricane for more than four days. Eventually, deteriorating ocean and atmospheric conditions caused Hilary to weaken as it continued to move west-northwestward towards the eastern portion of the basin.

The Southwest Pacific basin saw slightly reduced TC activity despite the anomalously elevated TCHP (Fig. 4.27). Nonetheless, three Category 4–5 TCs (Atu, Wilma, and Yasi) occurred in this region. Highlighted

in Fig. 4.29c, Severe Tropical Cyclone Yasi, which was observed to rapidly intensify over high values of TCHP (> 50 kJ cm^{-2}) made landfall as a strong Category 4 TC in northern Queensland, Australia (see section 4d7*ii* above).

In the WNP, all of the Category 4 and 5 TCs were observed to intensify over high values of TCHP (typically > 75 kJ cm^{-2} in the western North Pacific) except for Typhoon Roke. Roke was observed intensifying over lower TCHP values (~40 kJ cm^{-2} – 50 kJ cm^{-2}). However, this was a relatively fast-moving typhoon, traveling at around 7.5 m s^{-1}, as it intensified to its peak at Category 4. As fast-moving TCs induce less storm-induced cooling, they tend to intensify over relatively lower TCHP regions (Lin et al. 2009b). During the WNP typhoon season, 10 typhoons reached Category 1 intensity and 60% of these reached either Category 4 or 5 status, which is the highest percentage of Category 4–5 typhoon occurrence since 2007[8]. Among these, Super Typhoon Songda was first identified on 20 May, and from 24–26 May was over an area of high TCHP (> 100 kJ cm^{-2}), and rapidly intensified to a Category 5 TC, at a rate of 37 kts day^{-1} (19 m s^{-1} day^{-1}; Fig. 4.29d). Between 2005 and 2011, this was the only Category 5 typhoon that occurred during the month of May over the WNP.

The high TCHP of values > 100 kJ cm^{-2} observed in May 2011 suggests that the ocean provided sufficient energy for intensification (Lin et al. 2009a,b), along with other possibly favorable atmospheric conditions. Finally, in the WNP basin, Super Typhoon Muifa (Fig. 4.29e) was first observed on 25 July at latitude 5.6°N. After 4.5 days of genesis time, Muifa rapidly intensified, from Category 2 (85 kts or 44 m s^{-1}) to Category 5 (140 kts or 72 m s^{-1}) in only 12 hours on 30 July. This extremely rapid intensification rate, equivalent to 55 kts (28 m s^{-1}) in 24 hours is almost double the 30 kts (15 m s^{-1}) per day criteria for rapid intensification (Kaplan et al. 2010). It is noteworthy that this rapid intensification took place over an area with high TCHP values that exceeded 120 kJ cm^{-2}.

f. Intertropical convergence zones

1) Pacific—A. B. Mullan

The intertropical convergence zone (ITCZ) lies approximately parallel to the equator, with a slight poleward tilt on its eastern end, and varies in position from around 5°N–7°N in February–May to 7°N–10°N in August–November. The other major convergence zone, the South Pacific convergence zone (SPCZ), extends diagonally from around the Solomon Islands (10°S, 160°E) to near 30°S, 140W°, and is most active in the November–April half-year.

The Pacific began 2011 in a moderate to strong La Niña, which weakened through the first two quarters of the year to neutral conditions. A weaker La Niña returned in August 2011. Thus, the year was dominated by stronger-than-normal surface easterlies near the date line, cooler sea surface temperatures from the date line eastwards, and the convergence zones being further poleward than usual in both hemispheres, with an enhanced dry zone along the equator. A double ITCZ was present in March and April, with a fairly prominent southern branch

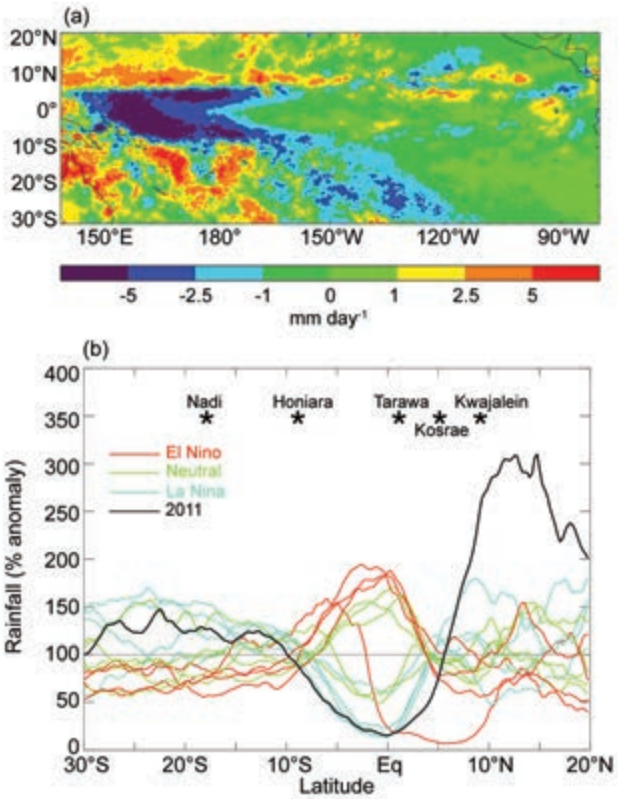

Fig. 4.30. (a) TRMM 3B43 rainfall anomaly for JFM 2011 (mm day^{-1}; relative to 1999–2008 mean); (b) Cross sections of JFM rainfall anomalies (% of 1999–2008 mean) for each year 1998 to 2011, averaged over sector 150°E–180°. Lines are colored according to ENSO status, except for 2011 (black). Stars mark latitude of selected island rainfall sites: Nadi (Fiji; 18°S, 175°E), Honiara (Solomon Islands; 9°S, 160°E), Tarawa (Kiribati; 1°N, 173°E), Kosrae (Micronesia; 5°N, 163°E), Kwajalein (Marshall Islands; 9°N, 167°E). The anomalous El Niño year is 1998.

[8] It should be noted that while both Songda and Muifa were briefly classified as Category 5 typhoons in the JTWC operational database, they were not officially classified as such by Japan Meteorological Agency, which is the official monitoring World Meteorological Organization center for the WNP.

between 150°W and 90°W, as is typical of La Niña years.

The poleward shift in the convergence zones was most clearly defined in the first quarter of the year (Fig. 4.30). Figure 4.30a shows the January–March rainfall anomalies relative to the Tropical Rainfall Measuring Mission (TRMM) 3B43 1999–2008 climatology. Reduced convection near the equator west of the date line is quite marked and the latitudinal extent of this enhanced dry zone was unusual even for La Niña conditions. Figure 4.30b demonstrates this by presenting transects of TRMM rainfall anomalies from 20°N to 30°S, averaged over the 150°E–180° sector. Even though the TRMM data cover a fairly short period (starting in 1998), there is a clear separation in the rainfall transects according to the ENSO status, which is determined here from NOAA's Oceanic Niño Index (ONI; http://www.cpc.ncep.noaa.gov/products/analysis_monitoring/ensostuff/ensoyears.shtml). (For the purpose of Fig. 4.30b, the quarter was classified as El Niño if two or more months exceeded the ONI +0.5°C threshold.)

In La Niña years, rainfall in the first quarter tends to be above normal poleward of about 8°S and 4°N, as an average over the 150°E–180° sector. The dry zone was more extensive in 2011, and the TRMM transects agree well with island rainfall records. Penrhyn (at 10°S) in the Northern Cook Islands received about 40% of its long-term seasonal rainfall and Tarawa in the western Kiribati Islands (near the equator) was exceptionally dry, at about 5% of normal (ICU 2011). North of the equator, Kosrae (at 5°N) in the Federated States of Micronesia received less than 75% of normal rainfall for the quarter (http://www.prh.noaa.gov/peac/update.php). Conversely, Fiji at 18°S and Kwajalein at 9°N were considerably wetter than normal. The rainfall anomaly north of about 8°N (Fig. 4.30b) appears exceptionally large, because January–March is normally the dry season in this part of the Pacific.

Figure 4.31 shows Pacific rainfall transects for all four quarters, divided into four longitude sectors. The Pacific transects are derived from the 0.25°-resolution NASA TRMM rainfall data (3B43 product; Huffman et al. 2007), except for July–December 2011 where 0.5° 3A12 data were used due to the current unavailability of 3B43. The 2011 positions of the convergence zones can be compared with the 1999–2008 climatology (see Mullan 2011 for the corresponding figure for 2010). The weak double ITCZ is evident in Fig. 4.31b.

The ITCZ and SPCZ are markedly poleward of their normal positions in January–March (first two panels of Fig. 4.31a). Thereafter, the peak ITCZ rainfall tended to occur near its normal latitude, or even equatorward in the second and third quarters as ENSO-neutral conditions prevailed. The SPCZ rainfall was displaced south of its normal latitude for much of the year. The SPCZ could also be described as being farther west than normal in the sense that a coherent convergence zone did not extend much farther east than 150°W. This is evident in Fig. 4.30a and also in the third panels of Figs. 4.31a–d. Thus,

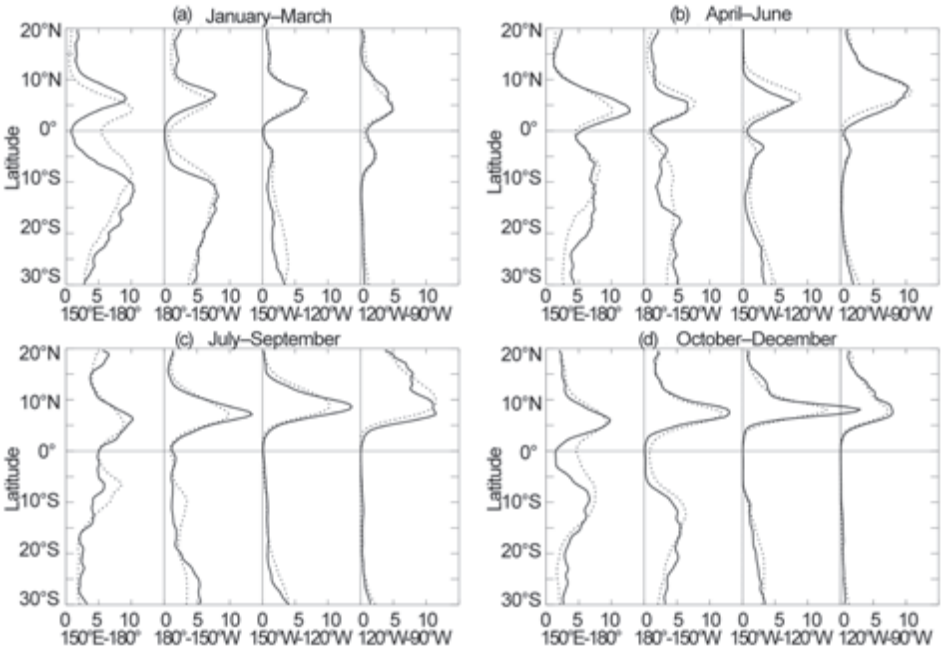

Fig. 4.31. Rainfall rate (mm day^{-1}) from TRMM analysis for the four quarters (a)–(d) of 2011. The separate panels for each quarter show the 2011 rainfall cross section between 20°N and 30°S (solid line) and the 1999–2008 climatology (dotted line), separately for four 30° sectors from 150°E–180° to 120°W–90°W. The climatology and 2011 rainfall in the first two quarters are from the TRMM 3B43 data, whereas the 2011 rainfall in the last two quarters are from TRMM 3A12 data.

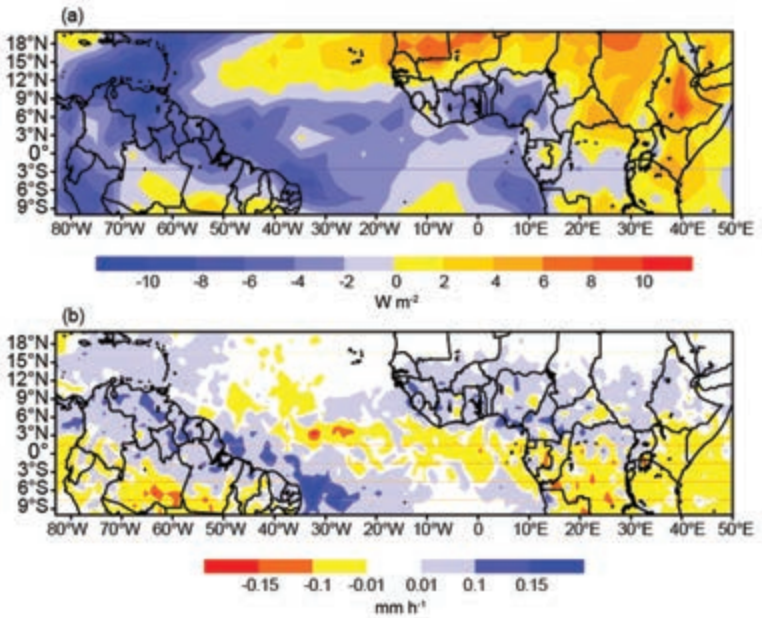

Fig. 4.32. (a) Atlantic NOAA-interpolated OLR (Liebmann and Smith 1996) anomalies (W m^{-2}) for 2011 and (b) TRMM anomalous precipitation rate (mm hr^{-1}) for Jan–Jun 2011. The anomalies were calculated based on the climatology for the period (a) 1975–2010 and (b) 1998–2010.

island groups south of the equator in particular tended to experience persistent rainfall anomalies for much of 2011, with an occasional respite during ENSO-neutral months. Tarawa (western Kiribati) and Penrhyn (Northern Cook Islands) had below-normal rainfall for 11 months of the year. Tahiti (French Polynesia), which lies farther to the east (150°W), received less than 50% of its normal rainfall for eight months of the year.

2) Atlantic—A. B. Pezza and C. A. S. Coelho

The Atlantic ITCZ is a well-organized convective band that oscillates approximately between 5°N–12°N during July–November and 5°N–5°S during January–May (Waliser and Gautier 1993; Nobre and Shukla 1996). Atmospheric equatorial Kelvin waves can modulate the ITCZ interannual variability (Mekonnen et al. 2008; Mounier et al. 2007) and ENSO is also known to influence the ITCZ on the seasonal time scale (Münnich and Neelin 2005). In 2011, the prevailing global scenario was that of a moderate-to-strong La Niña from January to April followed by yet another La Niña (weak to moderate) developing from September, with global climate anomalies typical of positive Southern Oscillation index (SOI) persisting in many areas of the globe. The ITCZ responded to this pattern and presented a noticeable enhancement, with negative average annual outgoing longwave radiation (OLR) anomalies in most of the equatorial Atlantic sector surrounding South America (Fig. 4.32a) driven primarily by the anomalous convection observed during the first half of the year (Fig. 4.32b). This pattern contributed to breaking the drought conditions

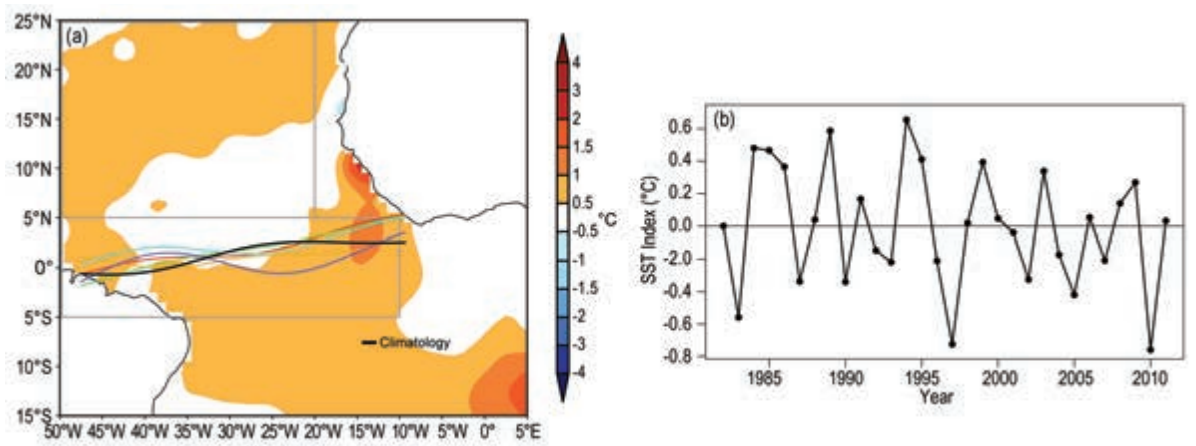

Fig. 4.33. (a) Atlantic ITCZ position inferred from OLR during March 2011. The colored thin lines indicate the approximate position for the six pentads of March 2011. The black thick line indicates the Atlantic ITCZ climatological position. The SST anomalies (°C, Reynolds et al. 2002) for March 2011 based on the 1982–2010 climatology are shaded. The two boxes indicate the areas used for the calculation of the new Atlantic Index in (b); (b) March SST anomaly time series (°C) averaged over the South American sector (5°S–5°N, 10°W–50°W) minus the SST anomaly time series averaged over the tropical coast of northern Africa (5°N–25°N, 20°W–50°W) for the period 1982–2011 forming the Atlantic Index. The positive phase of the index indicates favorable conditions for enhanced Atlantic ITCZ activity.

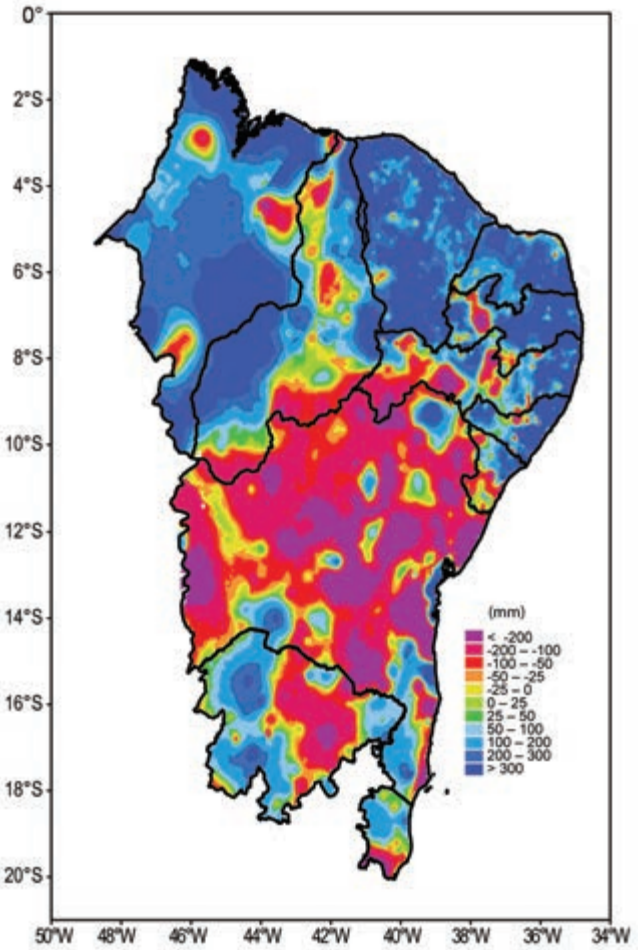

Fig. 4.34. Northeastern Brazil average 2011 precipitation anomaly (mm) with respect to 1961–90 climatology based on high-resolution station data. (Source: federal and regional networks CMCD/INPE, INMET, SUDENE, ANEEL, FUNCEME/CE, LMRS/PB, EMPARN/RN, LAMEPE/ITEP/PE, CMRH/SE, SEAAB/PI, SRH/BA, CEMIG/SIMGE/MG, and SEAG/ES)

that had previously been established in northeastern Brazil and parts of the Amazon in the previous year.

While the La Niña conditions indirectly helped enhance the ITCZ via Kelvin wave-induced upper-level divergence in the Atlantic sector, the demise of record-breaking warm SST anomalies observed over the subtropical North Atlantic (Fig. 4.33a) played a fundamental role via a favorable (enhanced) meridional SST gradient, expressed here by the Atlantic Index (see Fig. 4.33b caption for definition). A positive index in 2011, contrasting with the record-breaking negative index of 2010, implies a return to a more favorable pattern for frequent bursts of organized convection in the southern part of the basin and ultimately an overall enhancement of the ITCZ. Within this scenario, the ITCZ oscillated around its average climatological position for most of the year, with precipitation above average in parts of the eastern Amazon and northeastern Brazil (Fig. 4.34). This effect was due to the explicit dynamical response to upper-level divergence as well as the direct evaporative effect of the onshore trade winds responding to the north-south water temperature gradient, giving a typical La Niña response both in terms of positioning and strength of the ITCZ in 2011.

g. *Atlantic multidecadal oscillation*—C. Wang

The Atlantic Multidecadal Oscillation (AMO) is an oscillatory mode defined by the detrended North Atlantic SST anomalies over the region of 0°–60°N and from the east coast of the Americas to 0° longitude (Figs. 4.35a,b; Delworth and Mann 2000; Enfield et al. 2001; Wang et al. 2008a). A driving mechanism for the AMO may be the Atlantic meridional overturning circulation (Delworth and Mann 2000; Knight et al. 2005; Dijkstra et al. 2006; R. Zhang et al. 2007; see also section 3h of this report for detailed information on the meridional overturning circulation). A new study shows that the AMO varies with dust aerosol in the tropical North Atlantic and rain-

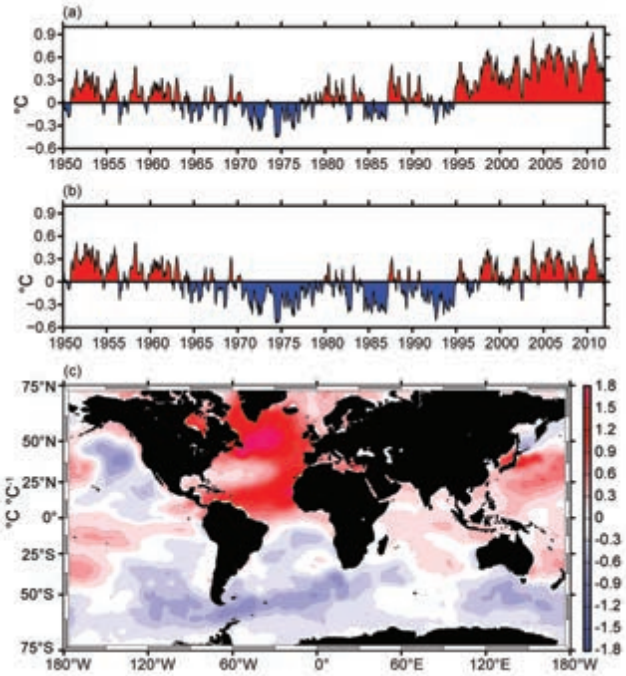

Fig. 4.35. The index of the AMO and its spatial pattern. Shown are (a) SST anomalies (°C) in the North Atlantic of 0°–60°N and from the east coast of the Americas to 0° longitude, (b) the AMO index (°C) defined by the detrended (removing the linear trend) North Atlantic SST anomalies, and (c) regression (°C per °C) of global SST anomalies onto the AMO index of (b). The monthly SST anomalies are calculated as departures from the 1971–2000 base period.

fall in the Sahel, suggesting that a positive feedback exists between North Atlantic SST, dust aerosol, and Sahel rainfall on multidecadal timescales (C. Wang et al. 2012). In addition to multidecadal variability, the AMO also demonstrates high-frequency variability such as an interannual variation via its connection to the tropical North Atlantic and the Atlantic Warm Pool (AWP; a large body of warm water comprising the Gulf of Mexico, Caribbean Sea, and the western tropical North Atlantic), and as such has exhibited a seasonal influence on the behavior of tropical cyclones (TCs) in the Atlantic and Eastern North Pacific (ENP) basins. The extended reconstructed SST (ERSST) data from 1950 to 2011 (Fig. 4.35b) shows that the AMO was in the cold phase from the late 1960s to the early 1990s and in the warm phase before the late 1960s and again after the early 1990s (Enfield et al. 2001). The AMO is related to SST anomalies over the global oceans as shown in Fig. 4.35c.

The AMO variability is associated with changes of climate and extreme events, such as drought and flood in North America and Europe, and hurricane activity in the North Atlantic and ENP (Enfield et al. 2001; McCabe et al. 2004; Goldenberg et al. 2001; Bell and Chelliah 2006; Wang et al. 2008a; Wang and Lee 2009). Recent studies show that the relationship of the AMO to TCs is due to its tropical component since the climate response to the North Atlantic SST anomalies is primarily forced at the low latitudes (e.g., Lu and Delworth 2005; Sutton and Hodson 2007). The AMO variability coincides with the multidecadal signal of the AWP and the AWP is in the path of, or a birthplace for, Atlantic TCs (Wang et al. 2008a). Thus, the influence of the AMO on climate and Atlantic TC activity operates through the mechanism of the AWP-induced atmospheric changes by having an effect on vertical wind shear in the hurricane main development region (MDR). A large AWP reduces such shear, while a small AWP enhances it. A large AWP also weakens the southerly Great Plains low-level jet, thus reducing the northward moisture transport from the Gulf of Mexico to the eastern United States and decreasing the boreal summer rainfall over the central US, while a small AWP has the opposite effect (Wang et al. 2006, 2008b). It has also been shown that the AWP variability can produce the observed out-of-phase relationship between TC activity in the tropical North Atlantic and ENP (Wang and Lee 2009).

As of 2011, the AMO has been in its warm phase since 1995. For all months in 2011, the North Atlantic SST anomalies were positive (Fig. 4.36a), with the maximum of the North Atlantic SST anomalies in January (+0.61°C) and the minimum in November (+0.30°C). Spatially, the North Atlantic SST anomalies during the boreal winter showed a tripole pattern with the positive SST anomalies in the subpolar North Atlantic and the tropical North Atlantic and the negative SST anomalies in the subtropical North Atlantic (Fig. 4.36b). The SST anomaly pattern divided the AWP into two parts: a colder Gulf of Mexico and a warmer Caribbean Sea/western tropical North Atlantic. The opposite SST anomaly pattern was consistent with a previous study (Muñoz et al. 2010), which showed that the air-sea fluxes as-

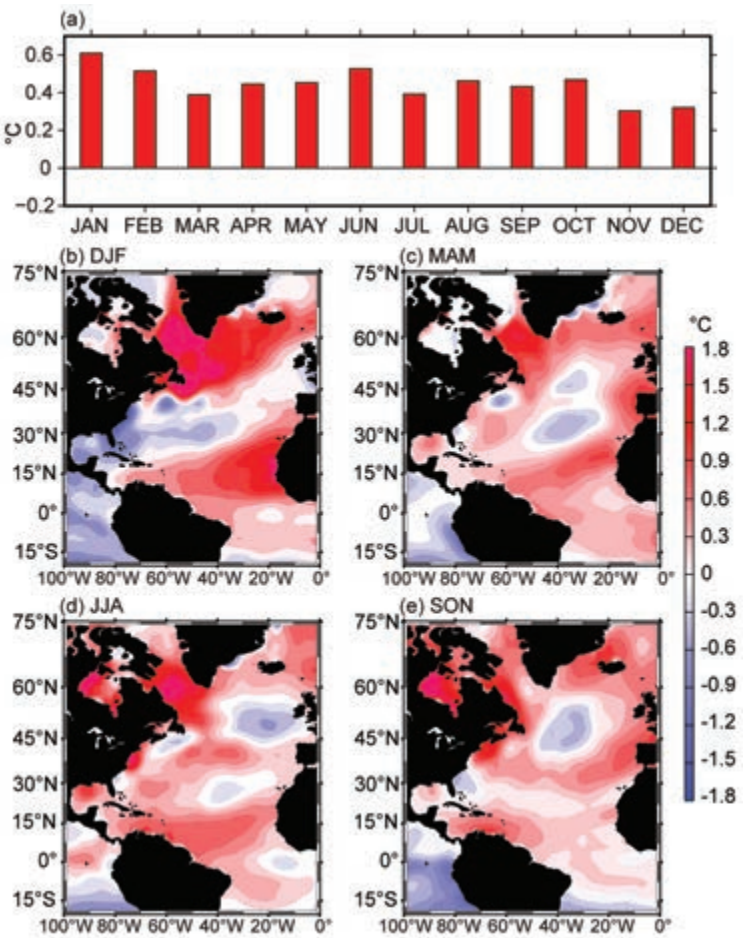

Fig. 4.36. The AMO in 2011. Shown are the (a) monthly North Atlantic SST anomalies (°C), (b) DJF 2010/11 SST anomalies (°C), (c) MAM SST anomalies, (d) JJA SST anomalies (°C), and (e) SON SST anomalies (°C). The monthly SST anomalies are calculated as departures from the 1971–2000 base period.

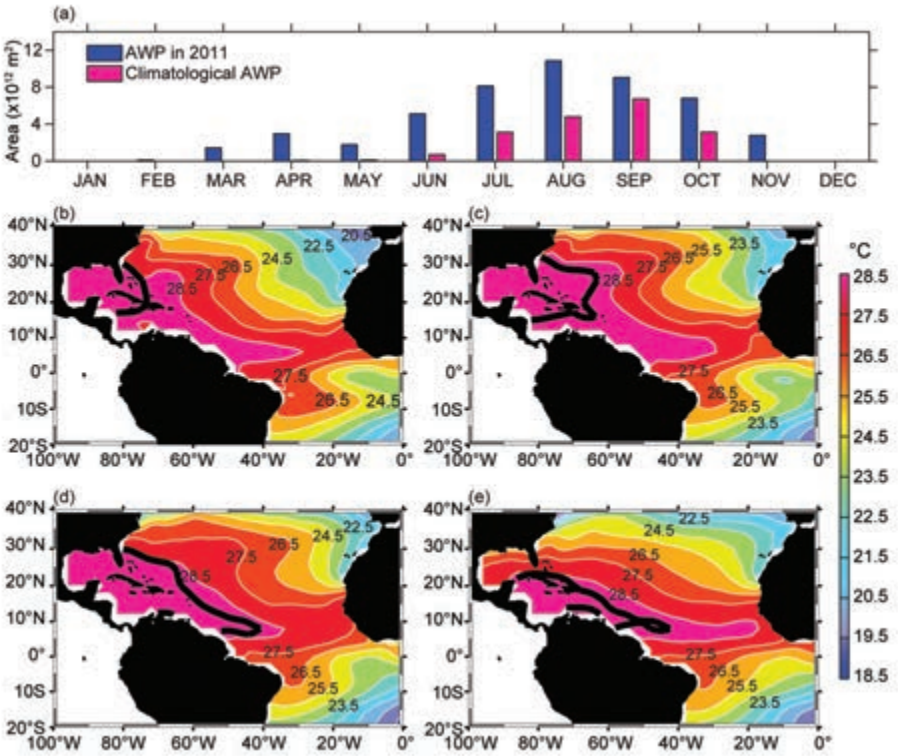

Fig. 4.37. The AWP in 2011. Shown are the (a) monthly AWP area in 2011 (10^{12} m^2; blue) and the climatological AWP area (red), spatial distributions of the 2011 AWP in (b) July, (c) August, (d) September, and (e) October. The AWP is defined by SST larger than 28.5°C. The black contours in (b)–(e) are the climatological AWP based on the data from 1971–2000.

sociated with ENSO events in the tropical Pacific and local processes were responsible for the SST anomaly distribution. During the boreal spring, summer, and fall of 2011, the cold SST anomalies in the subtropical North Atlantic weakened and the North Atlantic was mostly warm (Figs. 4.36c,d,e).

Previous studies have shown that the influence of the AMO on TC activity may operate through the atmospheric changes induced by the AWP or the Atlantic meridional mode (Wang et al. 2008a; Vimont and Kossin 2007). In particular, the AWP can play an important role in the hurricane track (Wang et al. 2011). During the 2011 Atlantic TC season of June to November, the AWP was consistently large (Fig. 4.37a) and the isotherm of 28.5°C extended eastward covering almost the entire tropical North Atlantic (Figs. 4.37b,c,d,e). An eastward expansion of the AWP shifted the hurricane genesis location eastward, decreasing the possibility for a hurricane to make landfall in the southeast United States. A large AWP also tended to shrink the North Atlantic subtropical high eastward (C. Wang et al. 2007) and produced a TC steering flow pattern along the Eastern Seaboard of the United States, which steered hurricanes away from the southeastern coast of the US (Wang et al. 2011). The large AWP in 2011 was also associated

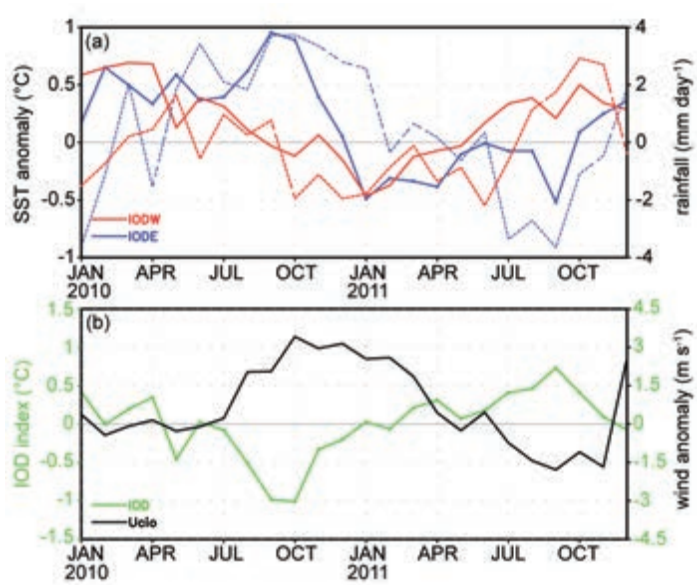

Fig. 4.38. (a) Monthly anomalies of SST (°C, solid lines) and precipitation (mm day^{-1}, dashed lines) in the eastern (IODE: 90E°–110°E, 10°S–0°; blue lines) and western pole (IODW: 50°E–70°E, 10°S–10°N; red lines) of IOD. (b) As in (a), but for the IOD index (measured by the SST difference between IODW and IODE, green line) and surface zonal wind anomaly (m s^{-1}) in the central equatorial IO (Ucio), from 70°E–90°E, 5°S–5°N, black line. The anomalies were calculated relative to the climatology over the period 1982–2010. These are based on the NCEP optimum interpolation SST (Reynolds and Chelton 2010), monthly GPCP precipitation analysis (http://precip.gsfc.nasa.gov/), and JRA-25 atmospheric reanalysis (Onogi et al. 2007).

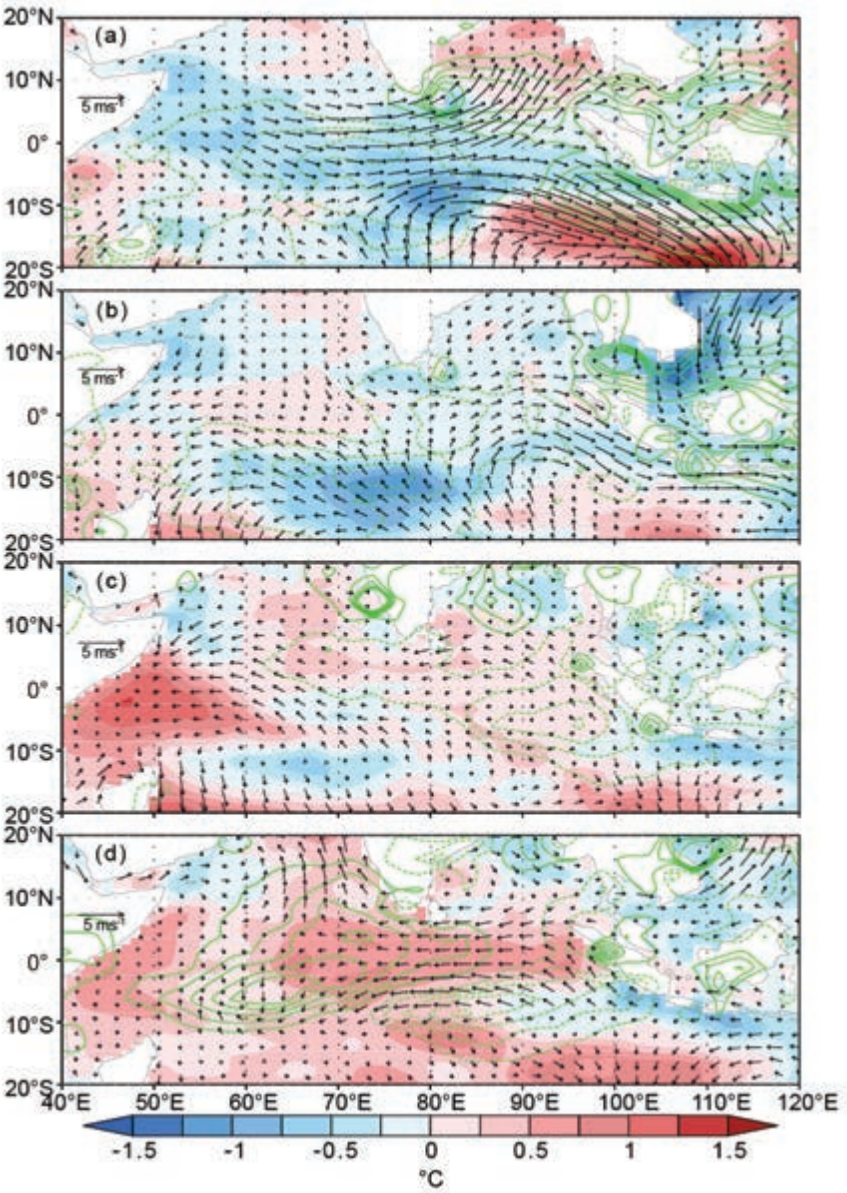

Fig. 4.39. SST (°C, colored scale), precipitation (green contours: ±1, ±2, …, ±5 mm day^{-1}). Solid (dashed) lines denote positive (negative) values, and surface wind anomalies during (a) DJF 2010/11, (b) MAM 2011, (c) JJA 2011, and (d) SON 2011.

with the out-of-phase relationship between TCs in the North Atlantic and the ENP as described previously in this chapter.

h. Indian Ocean dipole—J. J. Luo

The Indian Ocean dipole (IOD)—a climate mode in the tropical Indian Ocean (IO)—usually starts in boreal summer, peaks in fall, and decays rapidly in early winter. It has been believed that El Niño (La Niña) favors the development of positive (negative) IOD. During 2011, however, a weak positive IOD event occurred in the tropical Indian Ocean (Figs. 4.38 and 4.39d) in spite of the La Niña conditions in the Pacific. In particular, the cold SST anomalies in the eastern Indian Ocean were weak,[9] and the 2011 IOD was not well developed during its peak phase in SON compared to the past three strong positive IODs in 1994, 1997, and 2006. This is similar to what happened in 2007 and 2008 (Luo et al. 2008) and reconfirms the idea that the IOD can sometimes originate from the internal air-sea interactions in the IO (Behera et al. 2006; Luo et al. 2010). The strong La Niña event in 2010 helped to induce excessive surface westerlies in the central equatorial IO by enhancing the Walker cell in the IO. The westerly anomalies tend to cool the SST in the western IO by increasing surface latent heat loss from the ocean but warm the SST in the east by deepening the oceanic thermocline there; this favors the occurrence of a negative IOD in the second half of 2010 (Fig. 4.38). After the collapse of the negative IOD near the end of 2010, the excessive westerlies caused a cool/dry condition in most places of the tropical IO and a warm/wet condition in the Bay of Bengal and northwest of Australia during early 2011 (Figs. 4.38a, 4.39a). The related anomalous cyclonic winds in the southeastern IO raised the thermocline underneath and induced strong subsurface cooling and cold SST anomalies along ~10°S. The cold signals propagated westward but disappeared before they reached the western boundary of the IO (Figs. 4.39, 4.40). The drought

[9] Like an El Niño or La Niña event, a weak or strong IOD is defined by a threshold value of one standard deviation of the IOD index.

center in the IO gradually moved eastward and reached the eastern IO and Maritime Continent during June–August 2011 (Fig. 4.39c) which is typical of the weakening of the Pacific La Niña condition.

Cold SST anomalies started to develop near the coast of Java, Indonesia, in July 2011; this is closely linked with the southeasterly anomalies along the west coast of Sumatra, which could be partly driven by the north-south air pressure gradient associated with the dry center west of Sumatra and the wet center in the Bay of Bengal. The southeasterly anomalies raised the coastal thermocline and hence, induced the SST cooling. The colder-than-normal SST may, in turn, enhance the north-south pressure gradient and the southeasterly winds. As a result, both the SST cooling and southeasterly winds were enhanced quickly through this air-sea positive feedback. These signals expanded equatorward and westward and peaked in September 2011. There did not appear to be any subsurface cooling propagated from the western IO (Fig. 4.40a), suggesting that the local air-sea coupling in the eastern IO must have played a key role in generating the positive IOD event in 2011.

In the western IO, warm SST anomalies started to occur in May 2011 and grew rapidly in June–July 2011 in association with more surface solar radiation heating under less cloud conditions (Figs. 4.38a, 4.39c). The warm SST anomalies caused anomalous easterlies in the western IO during May–July 2011. In August 2011, the anomalous winds in the western IO and the east merged and led to basin-wide easterlies. This caused a pronounced dipole structure of precipitation anomalies, with flooding in the western IO and drought in the east during August–November 2011 (Fig. 4.39d). This dipole structure suddenly collapsed in December 2011 due to the strong westerly anomalies across the equatorial IO basin in association with the influences of both intraseasonal oscillation in the IO and the reenhancement of La Niña conditions in the Pacific.

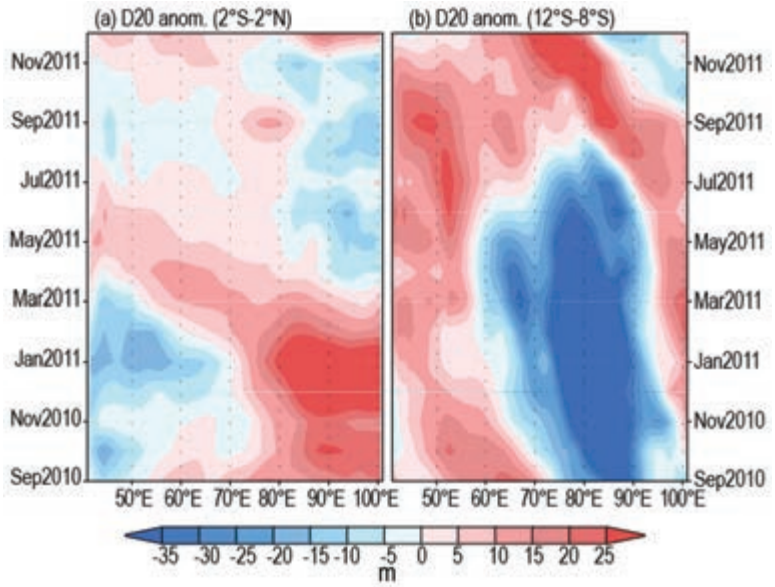

Fig. 4.40. 20°C isotherm depth (D20, m) anomalies in (a) the equatorial Indian Ocean (2°S–2°N) and (b) off-equatorial South Indian Ocean (12°S–8°S) in 2011. The data are derived from the NCEP ocean re-analysis available at http://www.cpc.ncep.noaa.gov/products/GODAS/.

SIDEBAR 4.1: MANAGING CLIMATE RISKS USING POLYNESIAN KNOWLEDGE—P. LEFALE, D. KING, AND A. NGARI

Long before the advent of numerical weather and climate models, Polynesian communities recognized that changes in biophysical phenomena could be used to forecast changes in local weather and climate conditions (Lefale 2010). Social, cultural, and traditional economic activities were planned and acted upon in response to these changes and revolved around the different seasons. Foremost among these was the capacity to forecast appropriate and inappropriate times for food gathering such as the planting and harvesting of crops and the catching of fish.

While weather and climate patterns have been monitored in the Southwest Pacific using Western scientific techniques since the late 1800s (1890 in Apia, Samoa, for example), little attention has been paid to the atmospheric observations and related expertise developed in-place by Polynesian people. However, recent work aimed at reaffirming Polynesian knowledge of weather and climate phenomena has shown that Maori, Cook Islanders, and Samoans possess their own unique local knowledge systems to forecast the onset of extreme events such as tropical cyclones and storms (Lefale 2003; King et al. 2007).

In Aotearoa/New Zealand, Maori have developed a detailed knowledge of biophysical processes and phenomena, including, among other skills, forecasting adverse weather and climate conditions (King et al. 2005). Ngati Koata, a tribal group from the north of the South Island, knew bad weather was imminent when stones were found in the belly of caught "*rawaru*" (blue cod). The stones are understood to give the *rawaru* ballast in the water as bigger waves and swell coincide with stormy conditions. Such indicators were not used in isolation, but rather as parts of a range of indicators that were (and continue to be) observed to confirm, via consensus, the forecast being made.

It is widely recognized in the Cook Islands, especially the southern islands, that a plentiful crop of mangoes typically indicates an active season of cyclones ahead (Fig. SB4.1). Knowledge of this phenomenon is common throughout the South Pacific region, from Vanuatu and Fiji in the west to Samoa and French Polynesia to the east. Migratory birds are also well recognized as indicators of severe weather, especially during summer. The "*torea*" (Pacific Golden Plover) is known to migrate between the Cook Islands and Alaska in the months of February–March and September–October, respectively (see http://cookislands.bishopmuseum.org/showarticle.asp?id=4). However, according to Mr. George "Birdman" Matearikі, a bird catcher on the island of Atiu, "*The birds on Atiu just disappeared in December [2004], and when those 5 cyclones came in from February 2005 for the Cook Islands, it dawned on me that the torea knew what would happen*" (Cook Islands government 2011).

Fig. SB4.1. A bumper mango season in Rarotonga, Cook Islands. Local indigenous knowledge indicates that the risk of tropical cyclones is still high for the nation. (Photo Credit: Mr. Arona Ngari, Director, Cook Islands Meteorological Service)

Fig. SB4.2. Widespread damage occurred in the village of Nikaupara on the island of Aitutaki in the Southern Cook Islands caused by Tropical Cyclone Pat in February 2010. (Photo Credit: Mr. Johnny Hosking in liaison with Air Rarotonga)

Similar biophysical indicators of change are used in Samoa. For example, the sudden appearance of cockroaches in large numbers in the evening during the cyclone season is understood to portend an approaching cyclone that can bring death and destruction (Fig SB4.2). Further, the appearance of frigate birds during a tropical cyclone signals the eye of the storm has arrived and that the worst of the storm is over. It is important to emphasize that the development and application of such knowledge was (and continues to be) fundamentally about managing climate-related risks linked with daily and seasonal changes in local weather and climate conditions (Cook Islands government 2006).

Reaffirming such knowledge provides an opportunity to understand what has assisted Polynesian people to cope and adapt to weather and climate variability in the past. It also provides lessons on how to deal with the risks associated with future weather and climate extremes (and related natural hazards), through greater awareness of the natural world and the inherent linkages between atmospheric and biophysical phenomena.

Libraries: Please file with the *Bulletin of the American Meteorological Society*, Vol. 93, Issue 7